NOVEL LIGHT-SENSITIVE NANOCRYSTAL SKINS

A THESIS
SUBMITTED TO THE INSTITUTE OF MATERIALS SCIENCE AND NANOTECHNOLOGY
AND THE GRADUATE SCHOOL OF ENGINEERING AND SCIENCE
OF BILKENT UNIVERSITY
IN PARTIAL FULLFILMENT OF THE REQUIREMENTS
FOR THE DEGREE OF
MASTER OF SCIENCE

By
Shahab Akhavan
July, 2013

I certify that I have read this thesis and that in my opinion it is fully adequate, in scope and in quality, as a thesis for the degree of Master of Science.

Assoc. Prof. Dr. Hilmi Volkan Demir (Supervisor)

I certify that I have read this thesis and that in my opinion it is fully adequate, in scope and in quality, as a thesis for the degree of Master of Science.

Assoc. Prof. Dr. Dönüş Tuncel

I certify that I have read this thesis and that in my opinion it is fully adequate, in scope and in quality, as a thesis for the degree of Master of Science.

Prof. Dr. Oğuz Gülseren

Approved for Graduate School of Engineering and Science

Prof. Dr. Levent Onural
Director of Graduate School of Engineering and Science

ABSTRACT

NOVEL LIGHT-SENSITIVE NANOCRYSTAL SKINS

Shahab Akhavan

M.S. in Materials Science and Nanotechnology

Supervisor: Assoc. Prof. Dr. Hilmi Volkan Demir

July, 2013

Light sensing devices traditionally made from crystalline or amorphous silicon, operating at the visible and near-infrared wavelengths, have led to a multibillion-dollar annual market. However, silicon faces various limitations including weak detection at long wavelengths (insufficient beyond 1.1 μm) with a cut-off at short wavelengths (in the ultraviolet) and small-area applications. On the other hand, solution-processed semiconductor nanocrystals (NCs), also known as colloidal quantum dots, offer large-area light sensing platforms with strong absorption cross-section. In this thesis we propose and demonstrate a new class of large-area, semi-transparent, light-sensitive nanocrystal skin (LS-NS) devices intended for large-surface applications including smart transparent windows and light-sensitive glass facades of smart buildings. These LS-NS platforms, which are fabricated over areas up to many tens of cm^2 using spray-coating and several cm-squares using dip-coating, are operated on the basis of photogenerated potential buildup, as opposed to conventional charge collection. The close interaction of the monolayer NCs of the LS-NS with the top interfacing metal contact results in highly sensitive photodetection in the absence of external bias, while the bottom side is isolated using a high dielectric spacing layer. In operation, electron-hole pairs created in the NCs of the LS-NS are disassociated and separated at the NC monolayer - metal interface due to the difference in the workfunctions. As a result, the proposed LS-NS platforms perform as highly sensitive photosensors, despite using a single NC monolayer, which makes the device semi-transparent and reduces the noise generation.

Furthermore, because of the band gap tunability, it is possible to construct cascaded NC layers with a designed band gap gradient where the NC diameters monotonically change. Here we present the first account of exciton funneling in an active device, which leads to significant performance improvement in the device. We show highly photosensitive NC skins employing the exciton funneling across the multiple layers of NC film. To further enhance the device photosensitivity performance, we demonstrate embedding plasmonic nanoparticles into the light-sensitive skins of the NCs. In addition, we exhibit the LS-NS device sensitivity enhancement utilizing the device architecture of semi-transparent tandem skins, the addition of TiO_2 layer for increased charge carrier dissociation, and the phenomenon of multiexciton generation in infrared NCs. With fully sealed NC monolayers, LS-NS is found to be highly stable under ambient conditions, promising for low-cost large-area UV/visible sensing in windows and facades of smart buildings. We believe the findings presented in this thesis have significant implications for the future design of photosensing platforms and for moving toward next generation large-surface light-sensing platforms.

Keywords: Quantum dots, nanocrystals, plasmonic nanostructures, TiO_2, multiexciton generation, light sensing, time resolved fluorescence, nanofabrication.

ÖZET

NANOKRİSTAL TABANLI IŞIĞA DUYARLI YENİLİKÇİ YÜZEYLER

ShahabAkhavan
Malzeme Bilimi ve Nanoteknoloji Yüksek Lisans
Tez Yöneticisi: Doç. Dr. Hilmi Volkan Demir
Temmuz, 2013

Günümüzde kristal veya amorf tabanlı silikondan yapılan ışığa duyarlı aygıtlar en çok kullanılan ışık sensörleridir. Bu aygıtlar görünür ve kızılötesi bölgelerinde çalışırlar ve yıllık birkaç milyar dolarlık bir markete sahiptirler. Fakat silikonun sınırlı malzeme özellikleriden dolayı, ışığa duyarlı aygıtlarda zayıf hassasiyete (kızılötesinde ve morötesinde) sahip olmaktadır ve üretim teknikleri sebebiyle bu aygıtlar sadece ufak alanlarda üretilebilmektedirler. Alternatif olarak, yarı iletken nanokristaller, aynı zamanda kolloidal kuvantum noktacıkları olarak da bilinirler, farklı ve üstün özellikleri ile son yıllarda ışığa duyarlı aygıtlar için ön plana çıkmış yenilikçi malzemelerdir. Bu tip nanokristaller solüsyon bazlı üretime ve işlemeye uygundurlar ve kuvvetli optik soğurmaya sahiptirler. Bu tezde yeni bir tip ışık sensörü olarak, büyük alanlı, yarı-geçirgen ve ışığa duyarlı nanokristal yüzeyleri tasarlıdık ve geliştirdik. Bu tip nanokristal yüzeyler (kısaltma olarak LS-NS'i kullanıyoruz) akıllı camlar ve akıllı bina cepheleri gibi geniş alanlı uygulamalara uygundur. LS-NS'ler onlarca cm^2 büyüklüğündeki alanlara sprey kaplması yöntemi ile, birkaç cm^2 büyüklüğündeki yüzeylere ise daldırmalı kaplama yöntemi ile kaplanabilir ve üretilebilir. LS-NS'lerin çalışma prensibi ışık ile elektriksel gerilim yaratımına dayanmaktadır ve bu klasik fotosensörlerin fotoakım yaratımı prensibinden farklıdır. LS-NS genel olarak paralel tabakalı kondansatöre benzemektedir. Üst metal katmanın altında tek bir nanokristal katmanı içerir. Alt iletken kısım ise optik geçirgendir ve nanokristal katmanında dielektrik sabiti yüksek bir yalıtkan

ile ayrılmıştır. Nanokristal katmanının üst metal ile etkileşimi sayesinde dışarıdan bir gerilimi uygulamaksızın yüksek ışık hassasiyeti elde edilir. Işık ile nanokristallerin içinde oluşturuluan elektron-deşik çiftleri metal-nanokristal arayüzeyinde farklı metal ve nanokristalin farklı elektonegativiteleri sebebiyle bir birinden kopar ve ayrışır ve bu ayrışma potansiyel fark, olarak ölçülebilir. LS-NS platformu tek bir nanokristal katmanı içermesine rağmen yüksek hassasiyette ışık duyarlılığına sahiptir, ayrıca yarı-geçirgen yapılabilir ve gürültü seviyesi azaltılabilir. Nanokristallerin ışıma dalga boylarının kolayca ayarlanabilir olması ile basamaklı yapıda nanokristal içeren dizaynlar yapılmasına olanak sağlamıştır. Bu sayede ışık ile oluşturulan elektron-deşik çiftleri yüksek enerjili nanokristallerden düşük enerjili nanokristallere doğru verimli şekilde aktarılabilmiştir. Bu tip eksiton taşınımı ilk defa aktif bir aygıtta bu tezde kullanıldı. Bu sayede eksiton taşınımını kullanan çok katmanlı nanokristal yapıları ile hassasiyeti artırılımış LS-NS'leri gösterdik. Aygıtların hassasiyetini daha da artırmak için plasmonik nanoparçacıkların katkılandırıldığı LS-NS'ler tasarladık. Yanı sıra yarı-geçirgen LS-NS'lerin ardarda dizilmesi ile birleşik aygıt yapıları ürettik, bunlara titanyum oksit katmanı ekleyerek yük ayrışımını artırılması sağldık. Ayrıca çoklu eksiton yaratımı prensibi ile kızılötesire hassas nanokristaller kullanarak verimlilik artışı gösteridik. LS-NS'ler tamamen izole edildiklerinden ortam koşullarından etkilenmediklerini ve karalı oldukları gördük. Tüm bu özellikler, LS-NS'leri ucuz, geniş alanlı ve ışık tayfına duyarlı (morötesi, görünür ve kızılötesi) ışık sensörleri yapmaktadır ve bu özellikleri onları akıllı camlarda ve akıllı bina cepheleri gibi alanlar için uygun yapmaktadır. Bu tezde gösterilen nanokristal tabanlı ışığa hassas yüzeyler gelecekteki ileri nesil ışık duyarlı platformlar için gelecek vaadetmektedir.

Anahtar kelimeler: Kuvantum noktacıkları, nanokristaller, plasmonik nanoyapılar, TiO_2, çoklu eksiton yaratımı, ışık hassasiyeti, zaman çözünürlü ışıma, nanofabrikasyon.

Acknowledgements

I would like to thank my supervisor Assoc. Prof. Dr. Hilmi Volkan Demir for his endless support during my professional experience with him. Through these years, I have learned a lot from him both technically and personally. I would like to thank him for his great contributions and guidance.

Also my special thanks go to Assoc. Prof. Dr. Dönüş Tuncel and Prof. Dr. Oğuz Gülseren for their kind support and also giving useful comments and suggestions as a member of my thesis committee.

This thesis would not be possible without our good friends and colleagues. First, I would like to thank all past and present Demir group members for being always helpful and friendly to me. Without your friendship and support, this thesis would not have been possible. I learned a lot from you and I am really proud to have such a selection of very nice people to be my best friends. Specially, I would like to thank Dr. Evren Mutlugün, Dr. Sedat Nizamoğlu, Dr. Emre Sarı, Burak Güzeltürk, and Talha Erdem from whom I have learned my basic lab skills and they always responded whenever I asked for help. I would like to acknowledge my friends Dr. Rohat Melik, Dr. Vijay Kumar Sharma, Dr. Dr. Ludwig P. Hernandez-Martinez and Dr. Urartu Ö. Ş. Şeker, Özgün Akyüz, Emre Ünal, and Dr. Nihan Koşku Perkgöz. And now comes my officemates. I cannot forget the happy times we had there. I would also very much like to acknolwledge Can Uran, Yusuf Keleştemur, Ahmet Fatih Cihan, Kıvanç Güngör, Aydan Yeltik, İbrahim Akcalı, Halil Akcalı, Mehmet Zafer Akgül, Sayım Gökyar, Akbar Alipour, Somayeh Fardindoost, Berkay Bozok, Ozan Yerli, Veli Tayfun Kılıç, Dr. Gökçe Küçükayan, Muammer Yasin Hacısalihoğlu, Erdal Gönendik, Mustafa Akın Sefünç, Yasemin Coşkun, Cüneyt Eroğlu, Onur Akın, Onur Erdem, and Togay Amirahmadov for their wonderful friendship and collaboration.

I would like to thank engineers and laboratory staff at UNAM who made our lives easier all the time.

I would also like to thank my parents for their endless love and support which helped me a lot to achieve my goals since my childhood. I would also like to thank my sister for always being kind to me and always next to me whenever I need her along with her enormous patience and love.

Table of Contents

List of Figures

List of Tables

To my parents who provided the opportunities and for their love, patience and understanding…

Chapter 1

Introduction

Imaging, remote sensing, optical communications, and spectroscopy are some of the important applications enabled by the detection of optical signals. A photosensitive material needs to absorb incident optical signals and convert them into electrical signals. Detection in the visible region is suitable for applications including spectroscopy and fluorescent biomedical imaging. In favor of the passive night vision [1, 2] and biomedical imaging for tumor detection [3, 4, 5] sensitive photodetection in the infrared region is required. Subsequently, multispectral imaging, which provides independent piece of information, is possible by combining visible and infrared wavelengths. However, due to the high fabrication cost and modest performance, their functionality is limited [6].

Light detection has traditionally been enabled by crystalline semiconductor photodetectors. In the last few decades, detectors made from silicon as photon-to-electron converter dominate the multibillion-dollar annual market [7]. The compatibility of the silicon electronics with silicon photodiodes enables low noise signal and multiplexing [8]. However, this technology faces some limitations. Silicon can absorb light relatively strongly only below 1.1 μm in addition to the weak absorption over the entire spectrum at 500 nm the absorption of silicon can only exceed 10^4 cm^{-1} [9]. Furthermore, silicon may also

suffer the cross talk and blurring of optical signal problems due to the long lifetime and high mobility of the electron-hole pairs [10]. Consequently, materials that expand the absorption spectrum with a high absorption coefficient to decrease the semiconductor thickness to at least less than 100 nm are significantly required.

Solution-processed semiconductor nanocrystals (NCs) are of increasing interest for use in optoelectronic devices and offer advantages including low cost, flexibility, large device area, and spectral tunability based on the quantum size effect [11, 12]. In contrast to conventional epitaxial growth of lattice-matched semiconductors, such solution-processed optoelectronic materials provide promising convenient integration atop electronic substrates (e.g., using dip coating, spin coating and drop casting), where lattice mismatch problems do not arise. Therefore, these NCs are promising candidates for applications in diverse areas, such as in light-emitting diodes [13], solar cells [14], and photodetectors [15, 16] as well as for biolabeling [17] and biosensing [18].

Conventional photodetectors using NCs typically operate on the principle of collecting photogenerated charges, where an external bias must be applied for the charge collection. Recent research efforts increasingly focus on NC photodetectors that show a remarkable level of sensitivity [19] and short response times [20]. These photodetectors do, however, commonly exhibit high dark current, which results in high noise levels and limits the device's detection capabilities [21].

Our research interest mainly focuses on fabricating and developing novel highly sensitive photosensor structure. As an alternative architecture, NC skins offer the potential of high sensitivity for large-area applications because they operate on the principle of photogenerated voltage buildup in the absence of an external bias. With a single NC layer in the device structure, noise generation is significantly reduced, which enhances the device sensitivity [22].

In Chapter 1, we present a brief introduction to materials and NCs for optical detection. The importance and the use of NCs in optoelectronic applications are discussed here.

In Chapter 2, we provide a background on the nanostructured materials for photon detection. Furthermore, we introduce surface plasmon resonance of metal nanoparticles and the influence of size, shape and environmental medium on the plasmonic behavior. Hence, we present a brief background on the Förster resonance energy transfer and its mechanism.

In Chapter 3, we discuss the fundamental properties of NCs as promising materials for optoelectronic devices. Also, we explain the synthesis methods of CdTe NCs, along with their optical characterization.

In Chapter 4, we present and demonstrate a large-area, semi-transparent, light-sensitive nanocrystal skin (LS-NS) devices. These LS-NS platforms, which were fabricated over areas up to 48 cm^2 using spray-coating and several cm-squares using dip-coating, are operated on the basis of photogenerated potential buildup, as opposed to conventional charge collection. In operation, close interaction of the monolayer NCs of the LS-NS with the top interfacing contact, while the bottom one is isolated using a high dielectric spacing layer, results in highly sensitive photosensing in the absence of external bias application.

In Chapter 5, we show that plasmonic nanoparticles are strong candidates to improve the electron-hole pair generation in NC-based devices. In particular, NC photosensors exhibit low performance toward long wavelengths, due to low optical absorption of NCs. Here, to enhance the device photosensitivity performance, embedding silver nanoparticles into the light-sensitive skins composed of the monolayer CdTe NCs was demonstrated. The deposited plasmonic silver nanoparticles increased optical absorption of the NC monolayer and enhanced the device photosensitivity. Improvements in photosensitivity

over broadband (400-650 nm) spectral range were observed with a 2.6-fold enhancement factor around the localized surface plasmon resonance peak. To further predict the enhancement in sensitivity of the devices, we performed simulations using FDTD method. Our experimental results agree well with the theoretical calculations considering the near-field electric field enhancement in the vicinity of silver nanoparticles. Furthermore, we studied the distance dependent sensitivity of the resulting devices with silver nanoparticles incorporated into NC skins to reveal the effect of localized surface plasmons.

In Chapter 6, we report the first colloidal NC-based tandem photosensitive skins. We fabricated the tandem photosensors which is composed of spray-coated monolayers of colloidal water soluble CdTe NCs and design the device to operate without applying any external bias. The top semi-transparent electrodes on each constituent junction accumulate holes while electrons are trapped inside the NCs. Subsequently, we have demonstrated that it is possible to enhance the device sensitivity for more that 100% and at the same time accelerate the response time compared to the single junction photosensitive devices.

In Chapter 7, we present the first account of exciton funneling in an active device, which leads to significant performance improvement in the device. Here we show highly photosensitive gradient NC skins based on the exciton funneling across the layers of NC film. Previously, this concept was demonstrated using layered NC films in the pioneering work of Franzl et al. [23]. To explore this proposition, we fabricated devices that rely on accumulating dissociated charges after photogenerating and funneling excitons. We demonstrate how funneling excitons along a gradually decreasing band gap gradient of the cascaded NC monolayers enhances photosensitivity of the device platform. We observed substantial improvements in the photosensitivity over a broadband spectral range (350-600 nm), with an approximately twofold enhancement factor along the entire operating wavelength range. To better understand and prove the presence of the exciton transfer process in the cascaded NC skins, we also

conducted time-resolved fluorescence measurements at the donor and acceptor wavelengths; the results confirmed the exciton transfer process in the NC gradient structure.

In Chapter 8, we show highly photosensitive NC skins based on the use of TiO_2 as electron accepting material. In the absence of any external bias, some excitons may remain in the NCs layer where it was created and then tend to recombine leading lower voltage buildup. To explore this proposition, we fabricated devices that rely on accumulating dissociated excitons after photogenerating and transferring electrons to TiO_2 while holes migrating to Al contact. As a result, we demonstrate how the electron transfer to TiO_2 thin film in LS-NS enhances photosensitivity of the device platform. We observed substantial improvements in the photosensitivity over a broadband spectral range (350-475 nm), with an approximately 22% enhancement. To better understand and prove the presence of the electron transfer process from the CdTe NCs to the TiO_2 layer, we also conducted time-resolved fluorescence measurements; the results supported the existence of electron transfer from the NCs to TiO_2 layer in light-sensitive skins.

In Chapter 9, we report a significant sensitivity enhancement making use of multiple exciton generation and subsequent charge accumulation per incident photon in photosensitive NC skins composed of a monolayer of near-infrared absorbing CdHgTe NCs. The 3.3-fold enhancement in sensitivity was observed at photon energies greater than 2.4 times of the CdHgTe NCs band gap. Implementing a control experiment, excitation of CdTe NC-based device did not show any enhancement through MEG due to the improper band gap of these NCs given the excitation wavelength.

Chapter 2

Scientific Background

2.1 Nanostructured Materials for Photon Detection

Colloidal semiconductor NCs, also known as colloidal quantum dots are made up of a few hundred to a few thousand atoms. Usually these materials are surrounded by an organic layer of surfactant molecules called as ligands [24, 25]. Their small size to a few nanometers (less than the Bohr radius) results in strong quantum confinement effect. This also increases the effective band gap due to the quantization of energy levels to discrete values. Subsequently, the sizes of the NCs influence their optical properties [26]. Optical properties of NCs also depend on their surface passivation. These surface passivated core NCs may result in surface trapped states acting as nonradiative channels reducing the fluorescence quantum yield. In order to improve the NCs' surface passivation, overgrowth with a shell of second semiconductor material has been the focus of significant research over the past two decades. It has been demonstrated that with coating the shell material it is possible to tune the emission and absorption spectra [27].

Regarding the band gap and relative position of electronic energy levels of the semiconductor, shell can have different functions. Electronic energy levels of bulk materials which are mostly used in NCs synthesis is given in Figure 2.1.1.

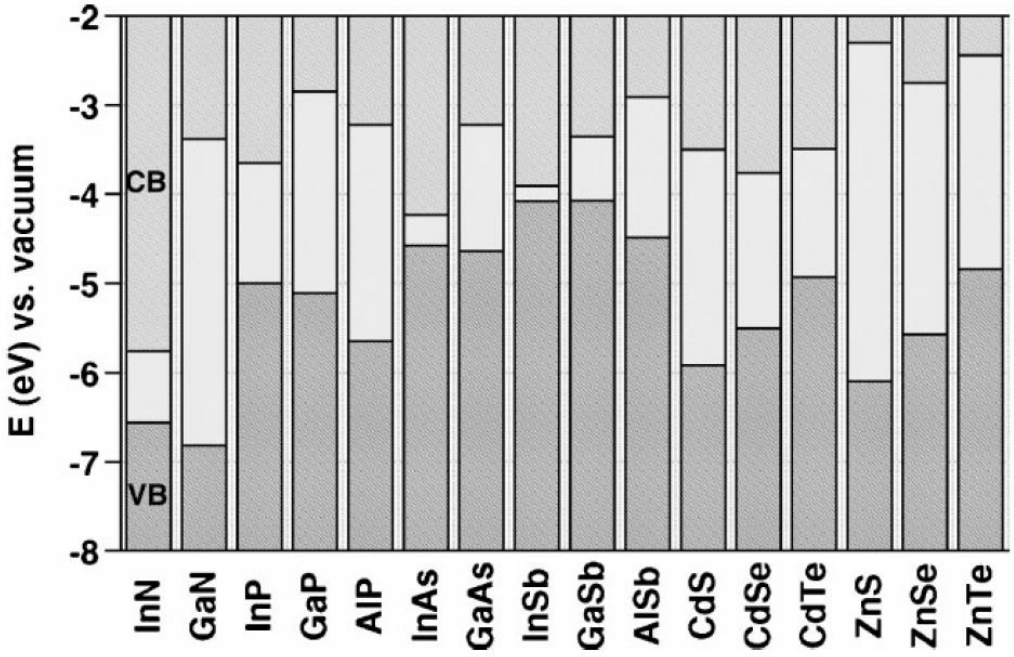

Figure 2.1.1 Energy levels of bulk materials which are mostly used in NCs synthesis [28].

Band alignment configurations can be distinguished in three cases known as type-I, reverse type-I, and type-II (see Figure 2.1.2). In the type-I case, when the band gap of the shell material is larger than the core, the electrons and holes are confined in the core. Usually, in order to passivate the surface of the core NCs which leads to improved emission, type-I is used. In this case, the shell passivates the core and reduces its dependency on the environmental changes such as oxygen or water molecules. Subsequently, stability of the NCs against photodegradation is enhanced. Moreover, the shell reduces the number of surface dangling bonds, which can act as trap states. In the reverse case, the band gap of the core material is larger than the shell one. Subsequently, depending on the shell thickness, electrons and holes are partially or completely confined in the shell. Subsequently, by changing the shell's thickness, the emission wavelength can be tuned [29, 30]. In these systems photostability can be enhanced by the growth of a second shell with a larger band gap [31]. In the last case, either the conduction-band edge or valence-band edge band gap of the shell is located in the band gap of the core. Because of the lower overlap of the

electron and hole wavefunctions, the photoluminescence (PL) decay of type-II is longer than type-I.

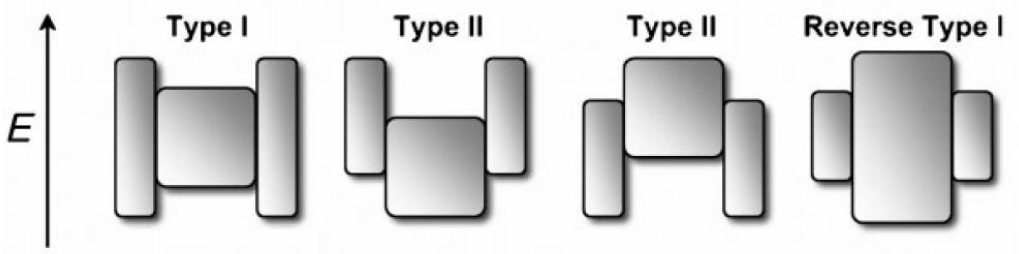

Figure 2.1.2 Energy-level alignment in three different core/shell cases [32].

For detection applications, NCs are attractive materials since they can easily be deposited with a variety of substrates. Although detectors made from silicon dominate the multibillion-dollar market for digital cameras and image sensors, they have some limitations. Silicon cannot absorb most of the infrared spectrum, since it absorbs wavelengths only below 1.1 μm. Moreover, it has a small absorption coefficient over the entire spectrum. Subsequently, materials that can absorb light where silicon cannot are of intense interest. However, these materials preferably need to be compatible for integration with silicon, flexible, and large-area substrates.

NCs offer great potential with their superior properties. They are very promising for optoelectronic devices including light emitting diodes [33], solar cells [34], single photon detectors and emitters [35], infrared sensors [36], light convertors [37, 38, 39], and scintillators [40]. NCs can be synthesized using wet chemistry and processed from the solution phase [41], which enables solution processable optoelectronic devices at reduced costs, with the additional advantages of making flexible structures, if desired, and in large-area production in principle. NCs are very versatile and can be deposited essentially almost on any substrate using dip coating [42], spin coating [43], spray coating [44], and inject printing [45]. Additionally, NCs possess widely tunable optical absorption and emission

properties using the quantum size effect. Moreover, the strong confinement leads to various mechanisms in NC solids including variable-range hopping [46], slow carrier relaxation [47], and electron and hole interaction [48] and delocalization [49].

Solution-processed photodetectors are classified into two classes, photoconductors and photodiodes. In the photodetectors, one type of the carrier circulates through the external circuit for several times until it recombines with the opposite trapped carrier, which leads to high gain. If the transit time is longer than the recombination duration of photogenerated excitons, many of charges can pass through the circuit. In order to prolong the electron-hole pair recombination time, introducing traps in the colloidal NCs film can be used [50, 51, 52]. The physical mechanisms behind solution-cast photoconductive photodetector have attracted great interest since 2006 [19]. In this previous study, PbS colloidal NCs were coated over prefabricated planar electrode array. The device showed a large photoconductive gain, especially after removing the ligands (see Figure 2.1.3).

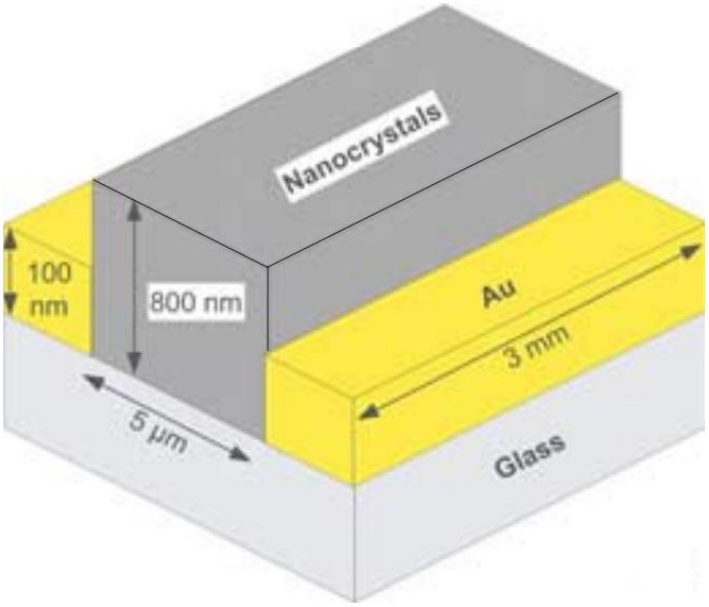

Figure 2.1.3 Device structure of ultrasensitive solution-cast quantum dot photodetector [19].

On the other hand, in the photodiodes, the photogenerated electrons and holes move to opposite electrical contacts (see Figure 2.1.4). These types of photodetectors can have fast response times. In photodiodes, difference in the material's Fermi levels leads to built-in potential. The internal field in the semiconductor depletion region separates the electrons and holes in opposite directions. To obtain high internal quantum efficiency, t_{life} should be larger than $t_{extract}$, where t_{life} is the lifetime of excess charge carriers and $t_{extract}$ is the time taken to transport carriers to the contacts given by $t_{extract} = L^2/\mu V_{bi}$ where L is the contact separation, μ mobility of slower carrier and V_{bi} is the built-in potential [53]. In conventional crystalline semiconductors, charges sweep a distance of 1μm much faster than nanoseconds through a built-in potential of 1 V, due to their high mobility, which is in the range of 10^2 cm^2Vs^{-1} and above. On the other hand, in solution-processed NCs charges sweep a distance of 100 nm with a built-in voltage of 1 V in the range of 100 ns-10 μs, since they have much lower motilities in the range of 10^{-5}-10^{-3} cm^2Vs^{-1}. However, thanks to the unusual long exciton lifetimes of some colloidal NCs (> 1μs), excellent photodiode quantum efficiency can be obtained [54].

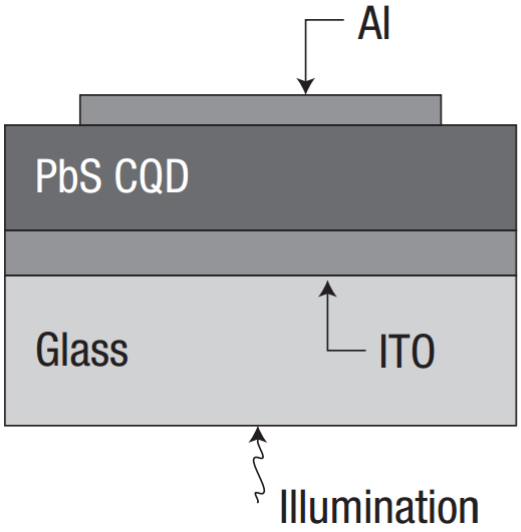

Figure 2.1.4 A schematic representation of the photodiode device architecture [21].

2.2 Fundamentals of Surface Plasmons

Localized surface plasmons (LSP) consist of the collective oscillations of free electrons spatially confined in metal nanoparticles under impinging electromagnetic radiation on resonance condition [55]. SP may appear in different forms such as freely propagating electromagnetic surface waves along metal surfaces and localized electron oscillations confined in metal nanoparticles. In this thesis, we will study the LSP generated in metal nanoparticles and used to enhance the device sensitivity in the spectral range especially where the photosensitivity is low.

The optical response of metal nanoparticles is due to the LSP resonance wavelength. As a result of SP, a strong electric field around the nanoparticle takes place, which vanishes exponentially by distance away from the nanoparticle [56]. LSP is strongly observed when the nanoparticle size decreases considerably, since electromagnetic field can penetrate into the particle. For Ag and Au metals, the penetration depth is around tens of nanometers. Subsequently, metal nanoparticles at this range should be obtained [57]. LSP generates polarization on the particle (sinusoidal varying electric field) and because of the Coulomb attraction force between the conduction electrons and fixed positive ions at the nucleus, a restoring force is generated [58]. As the electrons move back and forth, the restoring force gives rise to the oscillation (see Figure 2.2.1).

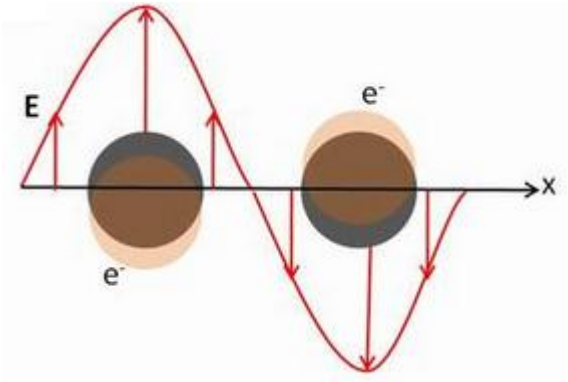

Figure 2.2.1 Schematic representation of the electric field due to an incident wave and creation of oscillation as the electrons move back and forth.

The frequency of this oscillation is called the SP resonance frequency. SP resonance is given as

$$w = \left(\frac{e^2}{\varepsilon_0 m_e 4\pi r_s^3} \right) \quad (1)$$

where ε_0 is the vacuum permittivity, m_e is the effective mass, r_s radius of sphere. As it is evident, resonance frequency is inversely proportional to the nanoparticle size [59].

LSP resonance frequency depends on the size, shape, and surrounding medium dielectric function. Ag and Au nanoparticles have frequencies corresponding to the visible region. On the other hand, Al and Hg have higher frequencies. The upper and lower size limits for Ag and Au to observe plasmonic effects is 100 and 5 nm, respectively. Ag and Au show strong SP resonance in the size range of 5-50 nm [60]. As the nanoparticle size increases, plasmon resonance makes red shift. Additionally, monodispersity of nanoparticle size distribution influences the plasmonic resonance peak. As the nanoparticles monodispersity increases, plasmon resonance peak become sharper. One of the other key factors effective on plasmon resonance is the shape of metal nanoparticles. They can be made in spherical, cubical and cylindrical. It has been reported that plasmon

resonance wavelength can be shifted from 400 to 670 nm as the spherical Ag nanoparticle changes to trigonal prism [61]. Moreover, different kinds of materials surrounding the nanoparticle can change the SP resonance spectrum. For example, the dielectric coating on film increase the refractive index of surrounding medium which cause a red shift in the plasmon resonance spectrum [62].

2.3 Förster Resonance Energy Transfer

Förster resonance energy transfer (FRET) is a nonradiative-type energy transfer that takes place between two resonance molecules in very close proximity. FRET has been especially used in biology to determine the distance between the molecules. In FRET, the donor molecule transfers its energy before being radiated as a photon emission. FRET occurs, when the donor emission spectrum overlap with the acceptor absorption spectrum. In this mechanism, the donor should have a high quantum yield, the acceptor should have a high extinction coefficient, and donor and acceptor should be in close proximity (less than 10 nm). In the case when the acceptor and donor molecules are less than 1 nm distance apart from each and, if their wavefunctions overlap, the exciton transfer occurs, which was first explained by the Förster theory.

To verify the Förster energy transfer, time resolved spectroscopy and steady state fluorescence measurement are used. In time resolved spectroscopy the mechanism is observed with the change in the donor lifetime. As the donor molecule feed the acceptor with its excitation energy, its lifetime decreases while the acceptor's increases. The rate of energy transfer has a r^{-6} dependency as given by Equation 2.

$$k_t = \frac{1}{\tau_D}\left(\frac{R_0}{r}\right)^6 \tag{2}$$

where K_t is the rate of energy transfer, τ_D is the donor lifetime in the absence of acceptor. R_0 is the Förster radius at which the decay rate and transfer rate of the molecule is equally probable and FRET efficiency is 50%. Förster radius can be found as follows:

$$R_0 = 0.211(\kappa^2 n^{-4} Q_D J(\lambda))^{\frac{1}{6}} \quad (3)$$

Here κ^2 is the orientation factor, n is the refractive index of the media, Q_D is the quantum efficiency of the donor, and J (λ) is the overlap integral. As it can be seen from the Figure 2.3.1 FRET is effective when r is less than or equal to R_0.

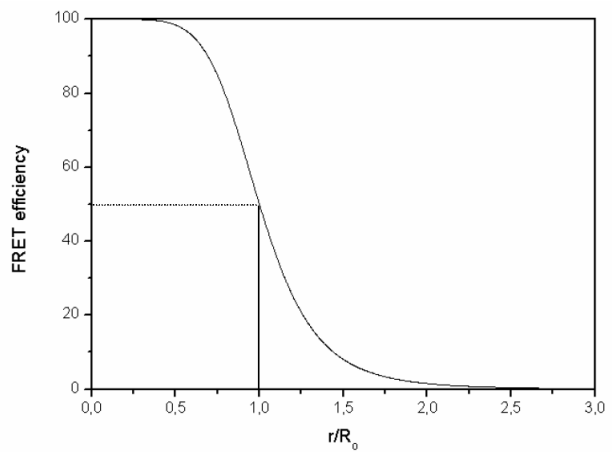

Figure 2.3.1 Dependence of the FRET efficiency on *r/R₀*.

Chapter 3

Semiconductor Nanocrystals

Chemically synthesized NCs are considered as candidate materials promising for a wide range of optoelectronic applications because of their band gap tunability and solution processability, which facilitate integration with a variety of substrates at reduced costs over large-areas. As a result, light detection using these colloidal NCs has attracted significant attention in recent years. Our research group is also interested in colloidal NCs containing the elements cadmium, indium, and selenium, which may also be surrounded by a shell composed of sulphur or zinc.

Generally, synthesis of semiconductor NCs results in spherical-like crystalline structures with diameters ranging from one to ten nanometers. When the electrons and holes are trapped in the potential well of the NCs in three dimensions, quantum confinement effect takes place. Moreover, on the contrary to the bulk crystalline semiconductor in which the energy level is continuous, the energy levels in NCs become discrete via the reduction of crystal size to nanoscale. Moreover, the exciton binding energy is given as follows:

$$E_n = \frac{\hbar^2 n^2}{8mr^2} \tag{4}$$

where ħ is the reduced plank's constant, n is the quantum number, m is the effective mass and r is the radius of NC.

Subsequently, the quantum size effect is the main reason for shifting the NCs emission as their size changes. For instance, we obtain red emission for the larger NCs, while the emission is blue for the smaller NCs.

3.1 CdTe Nanocrystal Synthesis

We synthesized water soluble (aqueous) CdTe NCs according to Ref [63]. In this method, 4.59 g of $Cd(ClO_4)_2.6H_2O$ was dissolved in 500 mL of Milli-Q water and 1.33 g TGA was added, followed by adjusting pH to 11.8-12.0. Then, H_2Te gas obtained from the reaction of 0.8 g Al_2Te_3 with H_2SO_4 was passed through the solution with a slow Ar flow. Subsequently, the nucleation and growth of the NCs was initiated at 100 ^{0}C. NCs start to grow as the solution starts boiling and gets bigger in size during this period. Synthesis setup used to synthesize CdTe NCs can be seen in Figure 3.1.1.

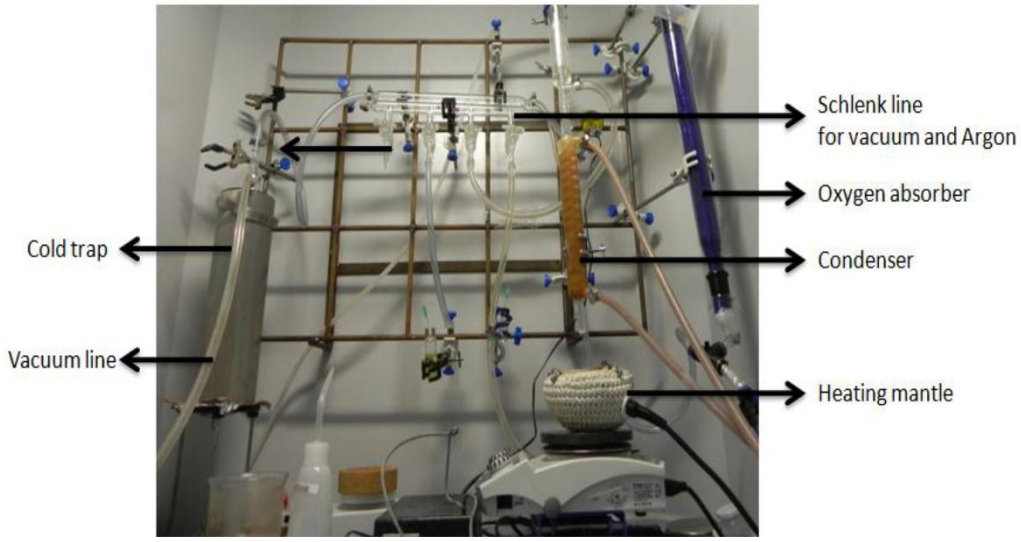

Figure 3.1.1 CdTe nanocrystal synthesis setup.

Fluorescence and optical absorption spectra of the resulting TGA-capped CdTe NCs are shown in Figure 3.1.2 and the NC diameters were calculated from their extinction spectra [32]. These diameters were 2.90, 2.98, 3.19, 3.62, and 3.71 nm, increasing the first excitonic peak wavelength as 525, 532, 545, 595, and 605 nm, respectively.

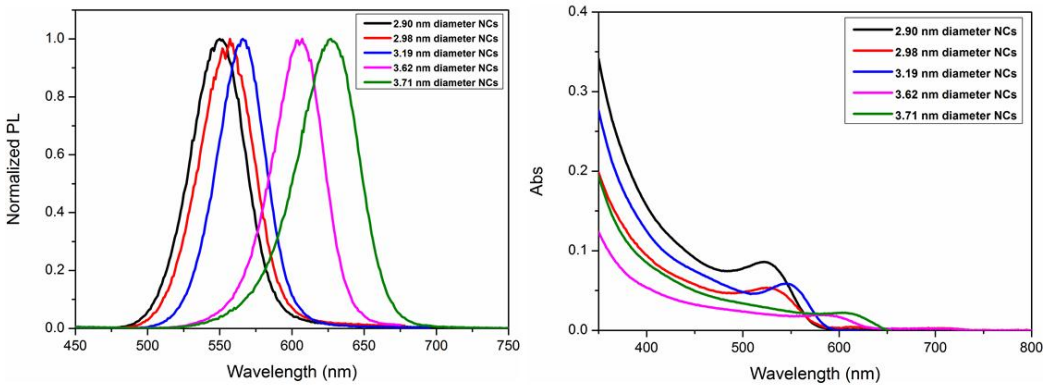

Figure 3.1.2 Photoluminescence and UV-vis absorption spectra of as-synthesized aqueous CdTe NC solutions at room temperature.

Furthermore, we found their photoluminescence decay lifetimes to be ~4 ns. After all, we use a rotary evaporator to increase the concentration and remove the extra amount of solvent. Hence, to further clean the solution from impurities, paper filters and size-selectively precipitation after several centrifuging steps are applied.

The control over the interface of NC surface is important because this helps to increase the device operation efficiency. Due to the ligands passivating the NC surface, charges see high potential barriers. To study the effect of ligands, we removed the TGA ligands from the NC surfaces by adding isopropanol into the CdTe NC solution and centrifuging the mixture. This process was carried out three times to remove sufficient ligands. During the layer-by-layer (LBL) film assembly, NC solution was then rigorously stirred in order to prevent the precipitation. The removal of the ligands from the NCs was confirmed by FT-IR spectroscopy. In the FT-IR spectrum, carbon-sulphur (C-S) bond is found to be

present in the TGA-capped CdTe NCs, whereas it is mostly absent after the cleaning step (see Figure 3.1.2), indicating the successful removal of the ligands.

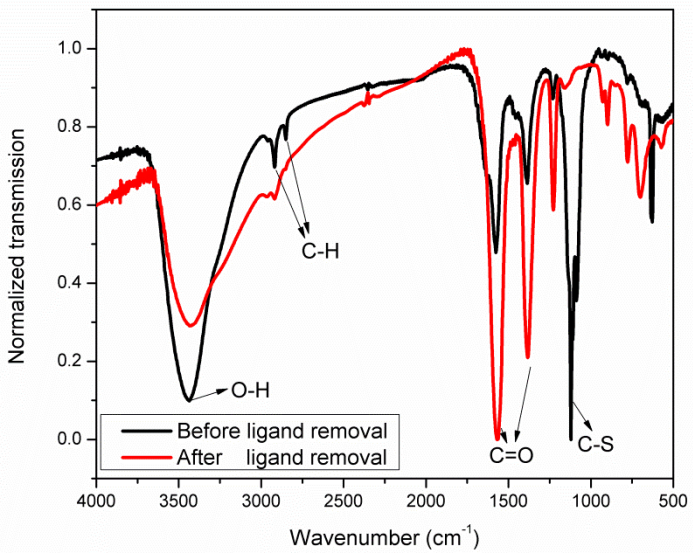

Figure 3.1.3 Normalized FT-IR spectra of TGA-capped CdTe NCs before and after the ligand removal.

3.2 Assembling of Semiconductor Nanocrystals

LBL deposition technique can be used for fabricating multilayered thin films with a fine control over the film thickness. The LbL assembly relies on alternating adsorption of oppositely charged species, e.g., positively and negatively charged polyelectrolyte pairs [64]. For the purpose of controlled NC deposition, the NC monolayer of LS-NS devices was prepared using LBL deposition. To make film deposition via LBL assembly, a fully computerized dip-coater system was used (see Figure 3.2.1). A monolayer of negatively charged CdTe NCs was deposited on top of alternating bilayers of strongly positive and negative polyelectrolyte polymers, deposited on HfO_2 layer, and followed by a final positive polyelectrolyte layer. Poly(diallyldimethylammonium chloride) (PDDA) and poly(sodium 4-styrenesulfonate) (PSS) were used as the positively and negatively charged

polyelectrolytes, respectively. The concentrations of these polyelectrolytes were 2 mg/mL in 0.1 M NaCl solution, since NaCl helps the polymer chain to relax on the surface. Water-soluble CdTe concentration was 4 μM. LBL films were prepared according to the standard cyclic procedure: (i) dipping of HfO_2-coated substrate into a PDDA solution for 5 min, (ii) rinsing it with water for 1 min, (iii) next dipping it into a solution of PSS for 5 min, and (iv) rinsing it with water for 1 min. This procedure was continued until four bilayers of PDDA and PSS composite were obtained. Finally, after deposition of one extra layer of PDDA and washing with water, the steps of dipping the sample into the dispersion of CdTe NCs for 20 min and rinsing with water again for 1 min were applied. Since the dip-coating technique has limitations for depositing CdTe NC monolayer on a large-area substrate, we employed spray-coating technique to paint NCs over large-areas, while keeping exactly the same sequence of monolayer depositions as described above.

Figure 3.2.1 Picture of our computerized dip-coater system.

Chapter 4

Large-Area Semi-Transparent Light-Sensitive Nanocrystal Skins

This chapter is based on the publication "Large-area semi-transparent light-sensitive nanocrystal skins," S. Akhavan, B. Guzelturk, V. K. Sharma, and H. V. Demir, *Optics Express*, 20, 25255-25266 (2012).

4.1 Introduction

Thin-film NC photodetectors based on photogenerated charge collection (using resultant photocurrent as the readout signal) have previously been proposed and successfully demonstrated in recent years, for which an externally applied bias is commonly required to extract the photogenerated charges [65]. In the conventional photodetection scheme, for increased sensitivity, it is necessary to use a thicker absorbing region so that a maximum amount of optical absorption takes place to give rise to the photocurrent. However, the thickness of the absorption region is restricted to few hundred nanometers (basically corresponding to many tens to hundreds of NC monolayers) due to the diffusion

length and short carrier lifetimes, which tends to decrease the photodetection sensitivity [66].

In this work, different than the previous reports, we propose and demonstrate a new class of large-area, semi-transparent, solution processed, light-sensitive nanocrystal skin (LS-NS) devices incorporating only one monolayer of NCs as the absorbing layer (see Figure 4.1.1). These LS-NS systems operate on the basis of photogenerated potential buildup internally across them rather than the charge collection, unlike common photodetectors [67]. The proposed LS-NS platforms perform as highly sensitive photosensors, despite using a single NC monolayer, though with a slow response. In operation, electron-hole pairs created in the NCs of the LS-NS are disassociated and separated at the NC monolayer-metal interface without applying any external bias. This leads to a voltage buildup, which decays with the RC decay of the whole circuitry mainly owing to the capacitive nature of the LS-NS device and the external shunt resistor connected to the device. These LS-NS devices can be fabricated over large areas at low cost, while providing high sensitivity to UV and visible light. Such LS-NS platforms are intended for use in large-area photosensitive windows and glass facades of smart buildings. These devices are not intended for applications that require a high operation speed. However, if desired, their operation can still further be extended to infrared (IR) range by selecting appropriate band gap of the NC sensing material (e.g., CdHgTe, PbS, and PbSe NCs).

The monolayer NCs used in the LS-NS are located immediately below the top metal contact enabling high sensitivity because of the close interaction with the metal contact while the other side of the NC monolayer is isolated using a thin stack of high-dielectric spacing layers. Only a small amount of NC material is used in the monolayer, which makes the LS-NS device semi-transparent (together with very thin top Al contact layer and transparent ITO contact layer on the bottom). The single monolayer of NCs, which is used to only partially

absorb the incident light, suffices to make the device highly photosensitive because it takes only a very small amount of charge accumulation for large enough photovoltage buildup. This NC single monolayer further enhances the sensitivity of the LS-NS device with reduced generation-recombination noise reduction [22]. It is worth noting that a single NC layer, such as the one used in LS-NS platform, would indeed make a very poor photodetector due to its very low optical absorption in the case of conventional photodetection scheme, in contrary to the highly sensitive LS-NS operation. Yet, as another important difference with respect to conventional photodetectors, there is no need for the LS-NS devices using an external power supply in a way similar to photovoltaic operation. This allows for potentially powerless operation of the LS-NS platforms in segments (each of which is under some detectable optical illumination as a whole).

In this work, we also demonstrate that it is further possible to fabricate large-area LS-NS conveniently by using the spray-coating method. This, in addition to being a low cost fabrication approach, results in a simple up-scalable technique for fabrication over extremely large areas. Also, the substrate on which the device is fabricated can be a flexible one, which makes it possible to fabricate fully flexible LS-NS devices. Moreover, the proposed NC photosensor structure allows for extremely high stability under ambient condition, since NCs are being sealed between the top metal contact and the bottom layers so that the NC monolayer is not exposed to air. With all these attractive features of high photosensitivity and photostability, and powerless operation, along with the possibility of large area and flexible implementations, the LS-NS platform holds great promise for three-dimensional wide-scale photosensing surfaces in the future.

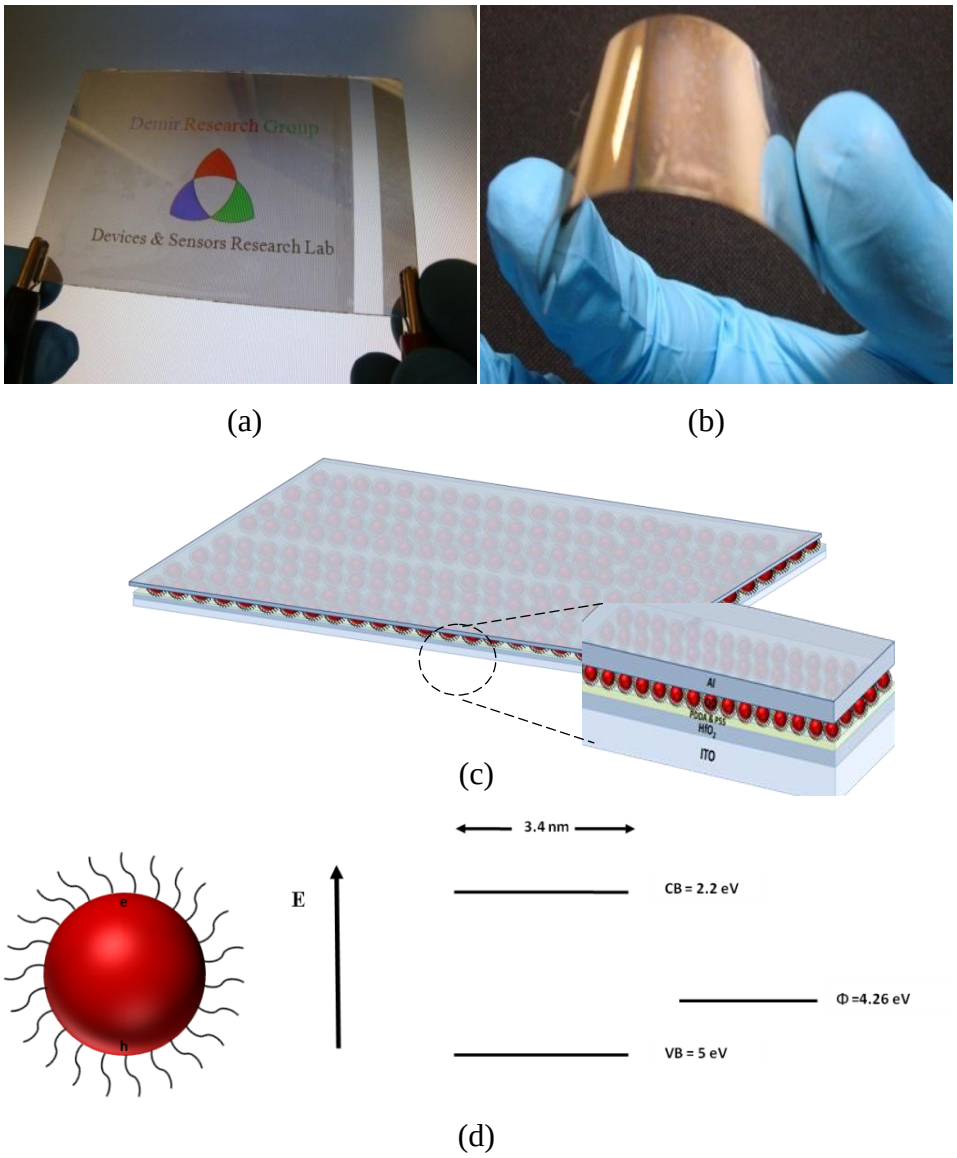

Figure 4.1.1 (a) Large-area, semi-transparent, solution processed, light-sensitive nanocrystal skin (LS-NS) devices. Here is shown a 8 cm × 6 cm LS-NS device. (b) Photograph of a flexible LS-NS. (c) Schematics of a LS-NS structure consisting of a monolayer of TGA-capped CdTe nanocrystals (NCs) (shown as a monolayer of red dots here), along with a zoom-in illustrating the device structure of ITO/HfO_2/PDDA+PSS/CdTe NCs/Al. (d) Band alignment of CdTe NCs and Al contact. CdTe NC conduction band (CB) and valence band (VB) and the workfunction (Φ) of Al are shown on the energy diagram.

As a proof-of-concept demonstration, we fabricated a semi-transparent LS-NS device of 8 cm × 6 cm (i.e., 48 cm^2) in size (see Figure 4.1.1(a)) in which the

maximum voltage buildup reaches 300 mV (under excitation at 350 nm with an optical power level of 0.153 mW/cm^2 without applying any external bias). To deposit a NC monolayer on the substrate, colloidal dots were painted onto the substrate using spray coating, followed by a washing step to guarantee the formation of a monolayer. By increasing the interaction with the top contact placed immediately above the NC monolayer, more charge accumulation took place, which expectedly led to the measured high photosensitivity. Thanks to the device architecture and utilization of solution processable NCs as the active semiconductor layer, our device has the potential to be constructed over even larger areas than the actual demonstrations here. LS-NS devices can also be made on a flexible substrate (e.g., ITO coated PET) if desired, as shown in a fabricated exemplary device in Figure 4.1.1(b). The device architecture of ITO/HfO_2/PDDA+PSS/CdTe NCs/Al is also sketched in Figure 4.1.1(c). Here the Al contact serves as the hole acceptor for the NCs given the workfunction of Al and the band alignment of the NCs shown in Figure 4.1.1(d). The experimental procedure and characterization results will be further discussed in detail in the following sections.

4.2 Experiments and Results

ITO film on a glass (or PET) substrate was washed using ultrasonication in a mixture of 2 mL Hellmanex in 100 mL water for 15 min, followed by ultrasonication in water (15 min), acetone (15 min) and isopropanol (15 min). Milli-Q water was used for all these steps and cleaning of the substrates. We then continued our fabrication by sputtering a 100 nm thick HfO_2 dielectric film. Subsequently, to deposit NCs, we used LBL self-assembly via dip coating to make a small device and spray coating to make a large device. At this step, we found that the formation of 4 bilayers of PDDA+PSS gives a uniform film with a high surface coverage for the subsequent CdTe NC monolayer. Following each self-assembly step, the sample was washed to remove excess and unbound species of the substrate. Finally, a transparent, very thin, Al contact layer (of 15

nm in thickness) was laid down immediately on top of the CdTe NC monolayer via thermal evaporation (see Figure 4.1.1(c)).

In our measurements, we used Agilent Technologies B1500A semiconductor parameter analyzer and Xenon light source with an integrated monochromator. The illumination intensity was measured with an optical powermeter (Newport multi-function optical powermeter). In operation, the devices were connected to a shunt resistor (for example, 200 MΩ, or other values of choice), and no external bias was applied across the device.

We performed electrical and optical characterizations of the LS-NS devices, including the measurements of photovoltage buildup, photodetection sensitivity, and photovoltage decay time. Because of the device architecture (sketched Figure 4.1.1(c)), electrical charges cannot directly pass through the device including the current blocking dielectric films (100 nm HfO_2 film and 4 bilayers of PDDA+PSS with full surface coverage) so that the LS-NS device itself acts as a capacitor. With light illumination on the device, excitons are photogenerated in the NCs. Following the exciton formation, excitons are dissociated at the NC-Al interface and the holes are transferred and accumulated at the Al side due to Al workfunction and HOMO/LUMO band alignment of the NC layer as shown in Figure 4.1.1(d). As a result, Al layer favors hole accumulation given the interfacing NC monolayer [26]. Therefore, in the LS-NS device, Al acts as a hole acceptor, which leads to positive charge accumulation in the top Al contact, while electrons tend to remain in the NCs. These charges are capacitively held across the device (stored charges); these are not trapped charges. However, due to the photocharging effect, some of the electrons are also trapped inside the NC deep trap states; these are long-lived trap states.

The operation of our device is experimentally shown in Figure 4.2.1. Starting the light illumination, we first observe that there is a net potential buildup and,

after reaching a peak point, this voltage buildup appears to diminish over time until it reaches a steady state in the presence of light illumination. At the steady state, when the light is switched off, a negative potential appears, which comes back to the initial point after short time. The observed operational mechanism of the LS-NS device is based on the photovoltage buildup rather than the immediate charge collection. This operation does not require external biasing. To understand the working of the device, it is worth mentioning that the non-trapped charges, which are held capacitively across the LS-NS device, are the stored charges, continuously decaying because of the shunt resistor with the RC decay of the whole circuitry (device + shunt resistor). There exist also trapped charges, beside the exponentially decaying stored ones. Simultaneously, the external circuitry tends to neutralize the trapped charges in the NCs for eventually obtaining charge neutrality across the device. With light impinging on the device, the transient response reaches a peak, at which these opposing components become equal to each other and balance each other. The net photovoltage buildup appears to decay after this point. The decay continues until the steady state is reached. By switching off the light at this steady state level (see Figure 4.2.1), the net potential goes negative. This is the potential of the trapped electrons.

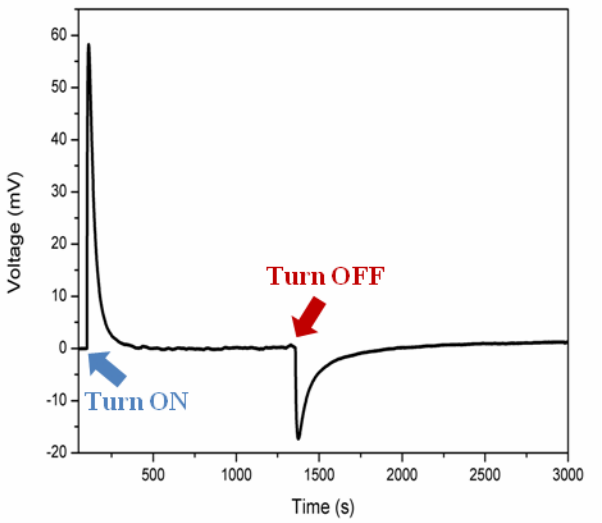

Figure 4.2.1 Changes in the voltage buildup in time via switching the incident light on and off (with 0.153 mW/cm^2 at 350 nm), marked with respective blue and red arrows.

While the light is on, some of the trapped charges draw holes from the Al contact to ensure the neutral state of the device. At the point when light is turned off, since there are no accumulated holes on the Al anymore, the net voltage reaches the lowest negative level and starts to recover and goes back to the zero level. This behavior shows the effect of trapped charges inside the NCs and the time taken to sweep out these charges. This indicates that the LS-NS device has a memory effect (within a certain time window).

As another interesting feature, LS-NS devices can also be used to give information directly about the total amount of incident light power impinging on the device within a certain exposure period of time. This corresponds to the total incident optical energy to which LS-NS has been exposed. We found that the magnitude of the negative voltage appearing after switching the light off, which is directly proportional to the number of trapped electrons inside the NCs, change accordingly in response to changing light exposure time. This is due to proportional photocharging during the period of light exposure as seen in Figure 4.2.2. However, this will work provided that the trap states in the NCs are not yet fully occupied and there are still more trap states available.

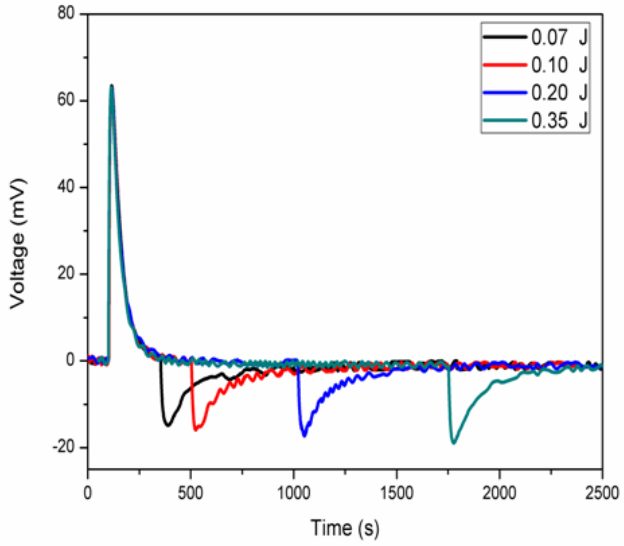

Figure 4.2.2 Effect of photocharge trapping inside the NCs as the incident light shines continuously on the nanocrystals skin for different periods of time at 350 nm (0.175 mW/cm^2). Here the total of incident optical energy given in the legend is the amount of incident optical power multiplied by the exposure time and the exposure area.

For a detailed understanding of the device operating principle, we further studied the LS-NS operation by systematically varying the excitation wavelength and illumination intensity. The voltage buildup variation in response to excitation with different intensities at different wavelengths is shown in Figure 4.2.3(a). We observed a higher voltage buildup at a shorter excitation wavelength, accompanied with a larger negative voltage after switching off the incident light. Due to the stronger optical absorption of CdTe NCs at shorter optical wavelengths, the voltage buildup is expected to increase with decreasing excitation wavelength. Essentially, this is because there are more electron and hole states available in a NC at a larger energy. This implies that a NC can absorb a larger number of photons at higher photon energies (i.e., at shorter wavelengths), photogenerating more electrons and holes under optical illumination at the same intensity level compared to longer wavelength excitation. This is in strong agreement with the profile of optical absorption spectrum of CdTe NCs.

We also observed that the device exhibits a larger negative voltage at a shorter excitation wavelength due to the increased number of trapped charges, again owing to the increased optical absorption. It also takes more time to relax this increased number of charges in the absence of light as shown in Figure 4.2.3(a). Similarly, Bulović et al. reported a decreasing external quantum efficiency of their cycled devices (NC-LEDs) as a result of charging of the NCs by trapped electrons over time [68]. We can measure the trap charge density in our devices, using the negative voltage value and the time required to recover after the light exposure is stopped.

Next, a meaningful figure-of-merit has been formulated to evaluate photodetection sensitivity of our device. Here we used the generic definition of the sensitivity as the ratio of electrical output signal to the optical input signal. Adapting this definition for the LS-NS devices, the photodetection sensitivity (S) is given by the ratio of photovoltage buildup to the incident optical power (i.e., $S=V/P$, where V is the photogenerated voltage (in V) and P is the optical power (in W) impinging on the device). Figure 4.2.3(b) presents the sensitivity of the LS-NS device as a function of the excitation wavelength, with an increasing trend towards shorter wavelengths in agreement with the discussions above.

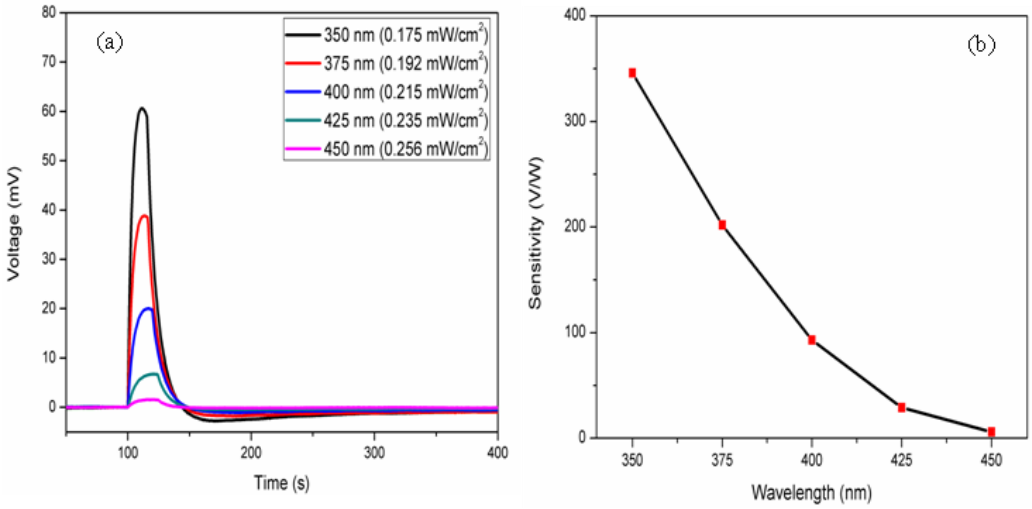

Figure 4.2.3 (a) Variation of the voltage buildup at different excitation wavelengths and intensity levels. Light was turned off after reaching the peak point. (b) Corresponding sensitivity curve of the LS-NS device as a function of excitation wavelengths.

We also studied the effect of varying incident power on the voltage buildup at a fixed wavelength (in this case, 350 nm). We observed that, with increasing power, the photosensitivity decreases while the response time grows shorter. This is because of the decreased RC, which means a faster response time and a decreased level of sensitivity (Figure 4.2.4).

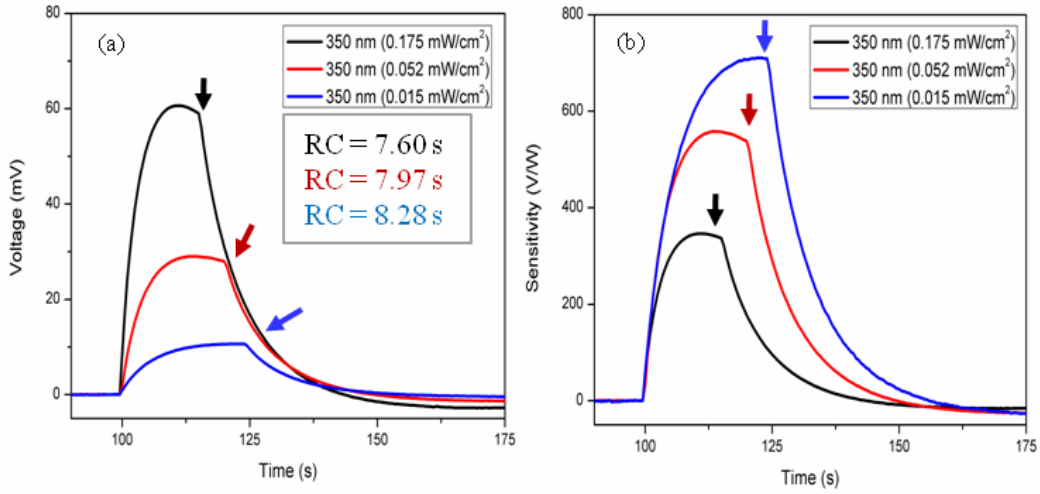

Figure 4.2.4 (a) Response time increases with the decreasing power since both deeper and shallower states saturate and (b) increasing illumination, resulting in decreased sensitivity because of filling the long-lived trap states. Arrows indicate the point in time when the light was turned off.

Furthermore, we observed that the RC decay kinetics changes over time in LS-NS devices (see Figure 4.2.5). While the shunt resistance (R) is fixed at 200 MΩ, the RC decay time constant decreases with time because of the change in the capacitance of the device. This change in the capacitance comes from the variation in the effective dielectric constant of the NC layer and thus the overall capacitance of the LS-NS device. The decreasing device capacitance can explain the reduced charge accumulation in the presence of light over time, which then results in a lower voltage buildup. Likewise, after reaching the peak point, the decrease in the device capacitance speeds up the RC decay, which is in correlation with the data summarized in Table 1.

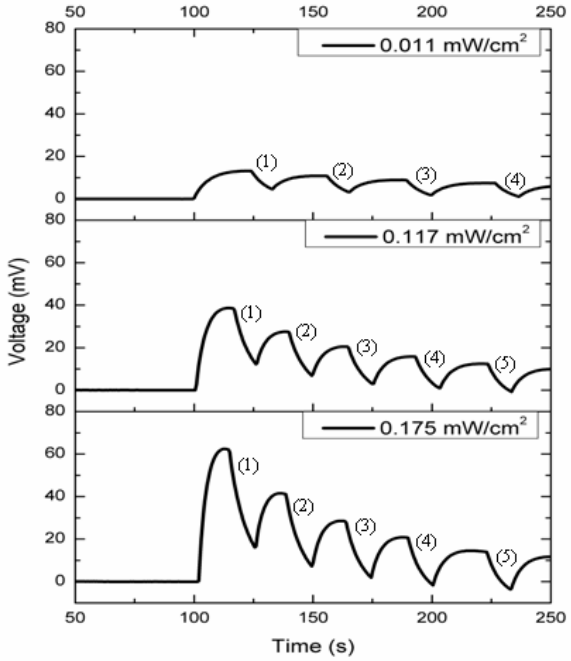

Figure 4.2.5 RC decay rate changing in time by turning the incident light on and off at different intensity levels at 350 nm.

Positions in Figure 4.2.5	P = 0.175 mW			P = 0.117 mW			P = 0.011 mW		
	τ (s)	C (nF)	ε_{CdTe}	τ (s)	C (nF)	ε_{CdTe}	τ (s)	C (nF)	ε_{CdTe}
(1)	7.56	37.80	5.3	7.76	38.80	8.6	7.91	39.55	16
(2)	6.57	32.85	1.6	6.93	34.65	2.2	7.53	37.65	4.9
(3)	5.24	26.20	0.7	5.95	29.75	0.9	6.82	34.10	2.0
(4)	4.65	23.25	0.5	5.06	25.30	0.6	6.08	30.40	1.1
(5)	3.62	18.10	0.3	4.34	21.70	0.4	5.64	28.20	0.9

Table 4.2.1 Various device parameters including RC decay time constant (τ), effective device capacitance (C), and effective dielectric constant of CdTe NCs (ε_{CdTe})) obtained from Figure 4.2.5, when the shunt resistance is fixed at 200 MΩ. P represents the excitation power level (of the Xenon lamp) incident on the device.

From Table 4.2.1, we observe that the illumination intensity changes the RC decay time constant. We found that the slowest one belongs to the lowest intensity level. This is in agreement with the potential buildup changing with the illumination intensity when the light illuminates the device continuously (Figure 4.2.6). The increased incident power results in a faster decrease, implying that the effective dielectric constant of NCs and thus the device capacitance are decreased. Therefore, the voltage buildup under higher power excitation drops faster after reaching the peak point compared to those at the lower optical intensity levels.

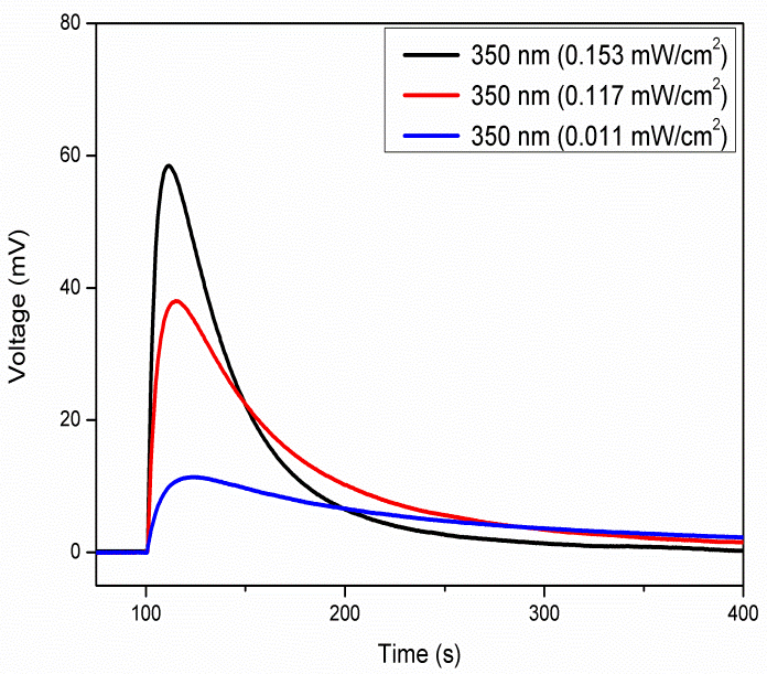

Figure 4.2.6 Variation of voltage buildup with time for different illumination intensity levels.

In the NCs, ligands act as the stabilizers by preventing them from aggregation and precipitation. However, when we make devices of these NCs, ligands can suppress the charge transport. It therefore makes sense to consider that the removal of ligands may increase charge transport and voltage buildup. This means that it is better to remove the ligands from NCs before making a device

out of them. To demonstrate the effect of ligand removal, the LS-NS devices were fabricated using ligand-removed CdTe NCs. It is found that these devices with the NC ligand removal exhibit a higher voltage buildup (104 mV), which indicates higher photosensitivity compared to the case of NC devices with the ligands (60 mV) at the same intensity level. This leads to a large sensitivity enhancement factor of 73%, together with a 3-fold faster response with respect to the case of using ligands. Ligand-removed NC devices also exhibit more trapped charges. Figure 4.2.7 shows that when ligands are removed, trapped charges can also be released much faster than the case with the ligands. Also, it is expected the change in the device capacitance be faster than the case with ligands, which is also confirmed experimentally in Figure 4.2.7.

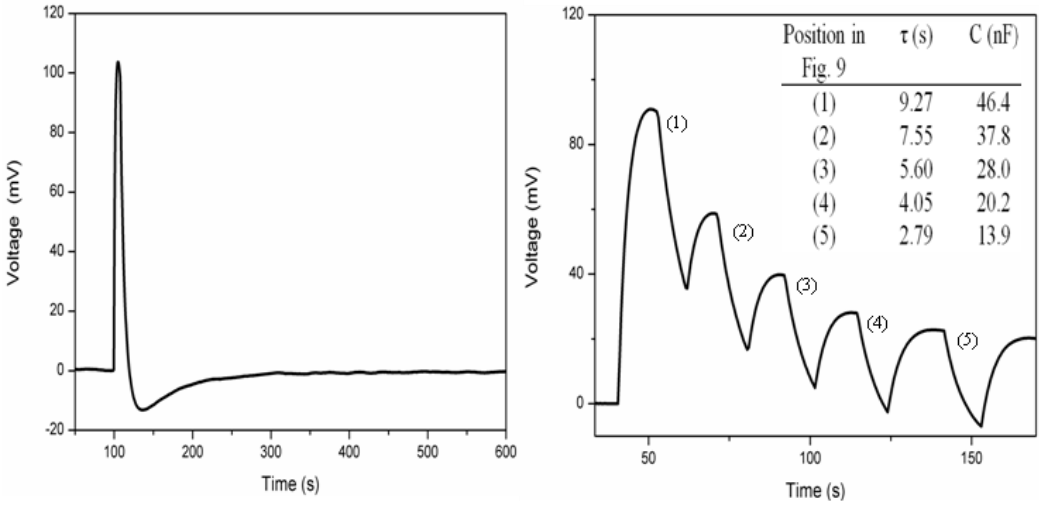

Figure 4.2.7 (a) Variation of voltage buildup with time for 0.175 mW/cm^2 at 350 nm and (b) RC decay change in time by turning the incident light on and off for 0.153 mW/cm^2 at 350 nm wavelength in the case of ligand-removed LS-NS devices.

Sensitivity and fast response time are desirable parameters for different photosensing applications. However, there is a tradeoff between them, and thus improving one worsens the other. For instance, for a device to be compatible with video-frame-rate imaging, a temporal response in the order of 50 ms is necessary. In the case of LS-NS devices, by decreasing the shunt resistance (e.g., from 200 MΩ, to 100 MΩ, 50 MΩ, 1000 KΩ, and 360 KΩ), it is possible to speed up the response time (from 8.0 s to 4.4 s, 2.4 s, 720 ms, and 300 ms,

respectively, for an excitation intensity of 0.175 mW/cm^2) as expected. For the same optical power, in the case of ligand-removed LS-NS devices, a faster RC decay time constant of 4.7 s, 2.4 s, 1.4 s, 220 ms, and 90 ms was observed. On the other hand, by increasing the shunt resistance (which was set to ~ 200 MΩ in our previous characterizations) would in fact enhance the sensitivity, but this would come at the cost of slowing its temporal response time (due to the increased RC decay time constant). Therefore, the response time of LS-NS devices need to be adjusted in regards to the requirements of a specific application.

The LS-NS devices exhibit reasonably high photosensitivity in comparison to typical NC photodetectors. In the case of LS-NS devices, we calculate the minimum noise equivalent intensity to be 1.94 μW/cm^2 for the devices with the ligands and 0.443 μW/cm^2 when ligands are removed, which is comparable to the solution-cast NC photodetectors reported previously [69]. This, in addition to the adjustable response time, makes the LS-NS platform a promising one for photosensing applications.

Chapter 5

Plasmonic Light-sensitive Skins of Nanocrystal Monolayers

This chapter is based on the publication "Plasmonic light-sensitive skins of nanocrystal monolayers," S. Akhavan, K. Gungor, E. Mutlugun, and H. V. Demir, *Nanotechnology*, 24, 155201 (2013).

5.1 Introduction

NCs exhibit low optical absorption in the long wavelength range, which limits the device performance. Here, to enhance the sensitivity and extend operating wavelength range, embedding silver nanoparticles into LS-NS is proposed and demonstrated. LSP consists of the collective oscillations of free electrons spatially confined in metal nanoparticles under impinging electromagnetic radiation on resonance condition. LSP resonance wavelength depends on the material, shape and size of the nanoparticle as well as the surrounding medium dielectric function [70]. Around the LSP resonance peak exponentially decaying, evanescent fields are localized in the vicinity of silver nanoparticles, which may yield an order of magnitude field localization enhancement. Consequently, this field enhancement promotes the optical absorption and electron-hole pair generation of plasmonically coupled active layer [71, 72].

Introduction of plasmonic materials into light harvesting devices can substantially enhance the exciton photogeneration [73, 74].

Silver nanoparticle-enabled plasmonic effect has been made in variety of ways to enhance the performance of thin film based optoelectronic devices. M. L. Tseng et al. have proposed a fast technique for the development of Ag nanostructure from AgO_x thin film deposited on a glass substrate via a femtosecond laser which can be applied over large areas [75]. Similarly, low cost, simple and novel nucleated silver nanoparticles has been demonstrated to broadband absorption enhancement in thin-film amorphous silicon solar cells [76]. In this work we employed LSP effect of silver nanoparticles to engineer plasmonic absorption profile for enhancing electron-hole pair generation in CdTe NCs. This enhancement leads to increased sensitivity and broadened operational spectral region of the LS-NS devices. Careful tailoring of the plasmonic absorption profile enables further optimized device performance. Therefore, the integration of monolayer NCs film with silver nanoparticles offers great potential to become a promising low cost light-sensitive platform for UV/visible sensing [77].

5. 2 Device Preparation and Characterization

To obtain localized plasmonic nanostructures, we deposited silver nanoparticles on 50 nm thick HfO_2 dielectric layer of our LS-NS devices using a thermal evaporator at a reduced evaporation rate of 0.3 Å/s in vacuum environment. As a result of such a low evaporation rate and small mass thickness, nanometer size islands of silver isolated from each other were obtained. After the evaporation, the samples were annealed at different temperatures and for different durations (150 °C for 2 min, 300 °C for 2 min, and 300 °C for 20 min) to further allow the silver nanoparticles to reorganize into the desired morphology. In this method, the four main parameters that determine the size and organization of the silver nanoparticles include evaporation rate, thickness, annealing temperature, and

duration. During the process of developing these silver nanoparticles, different mass thicknesses and evaporation rates (not presented here) have been systematically studied. Consequently, the best results were achieved with 10 nm mass thickness and 0.3 Å/s evaporation rate as the optimal case, which gives the sharpest peak and narrowest full-width-half-maximum (FWHM) in addition to the desired LSP resonance. Scanning electron microscopy (SEM) images of four silver films deposited with a film mass thickness of 10 nm on the HfO_2 substrate and annealed at different temperatures and for different durations are shown in Figure 5.2.1. Here it can be seen that heat treatment helps the silver nanoparticles to reorganize themselves such that they become more isolated from each other and more spherical in shape.

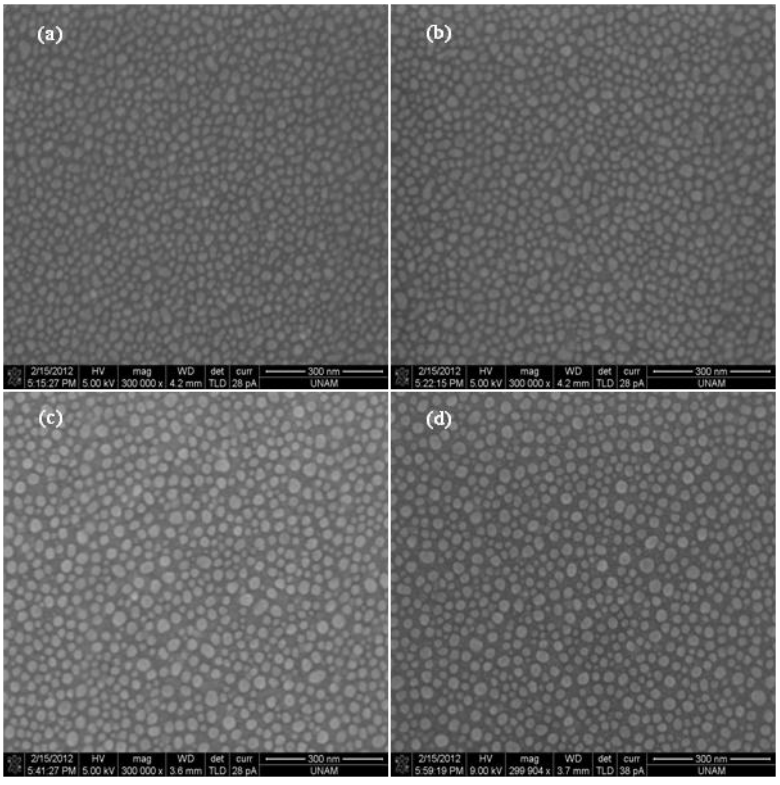

Figure 5.2.1 SEM images of four silver nanoparticle films with 10 nm mass thickness on a 50 nm thick HfO_2 film annealed at different temperatures and durations. (a) Not annealed, (b) annealed at 150 °C for 2 min, (c) annealed at 300 °C for 2 min, and (d) annealed at 300 °C for 20 min.

Optical absorption spectra of the resulting silver nanoparticle films (see Figure 5.2.2(a)) are in agreement with the SEM images displayed in Figure 5.2.1. Stronger, blue-shifted LSP resonance with a narrow FWHM is observed from optical extinction spectra confirming the isolation and size reduction of nanoparticles. Later we shall discuss how this tunability of resonance peak enhances the device sensitivity in the range where photosensitivity is low. To facilitate layer-by-layer assembly of NCs, a 1 nm thick negatively charged aluminum oxide (Al_2O_3) layer was subsequently deposited using ALD onto the silver nanoparticle films. Depositing 1 nm thick Al_2O_3 and subsequently coating bilayers of PDDA and PSS polyelectrolytes onto the silver nanoparticle films did not make a significant change in the LSP resonance (see Figure 5.2.2(b)).

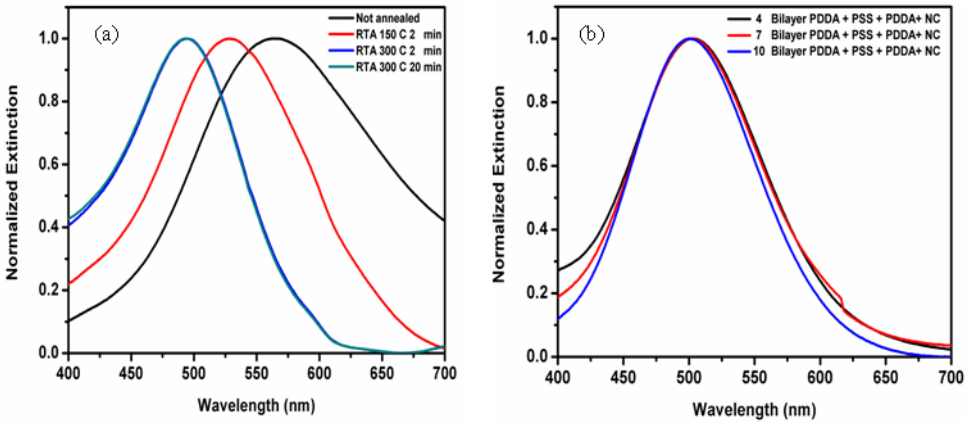

Figure 5.2.2 (a) Optical excitation spectra of silver nanoparticle films with a mass thickness of 10 nm deposited at 0.3 Å/s evaporated rate annealed at different temperatures for different durations. (b) Optical extinction spectra of 10 nm thick silver nanoparticle film annealed at 300 °C for 20 min covered with 1 nm Al_2O_3, different number of PDDA and PSS bilayers, and single monolayer of NC.

Figure 5.2.3(a) presents a schematic of the plasmonically enhanced LS-NS device, in which aluminum oxide and polyelectrolyte polymers separate silver nanoparticles and CdTe NCs. In our device architecture, charges are not allowed to pass directly through the device. After electron-hole pairs are photogenerated, because of the workfunctions of the NC monolayer [78] and Al layer (see

Figure 5.2.3(b)), holes migrate to the Al contact while most of the electrons are trapped inside the NCs. By shining light on the device, excitons are dissociated at the Al and NC monolayer interface. Subsequently, holes are migrated and accumulated at the Al side due to Al workfunction and band alignment of the NC monolayer. On the other hand, electrons tend to stay in the NCs because of presence of highly dielectric layer of HfO_2. Consequently, holes start to accumulate at the Al contact, making a positive potential buildup up to the saturation point. After a while, switching off the light results in decreasing the potential buildup. Hence, the device exhibits negative voltage value after switching off the light due to the trapped electrons inside the NCs. Furthermore, a higher voltage buildup is observed at a shorter wavelength indicating wavelength dependency of the device as a consequence of a larger number of states available at the shorter wavelength. This behavior is in strong agreement with the absorption spectrum of CdTe NCs. Furthermore, the voltage buildup as a result of trapped electrons is directly related to the negative voltage observed after switching off the light. In other words, a larger potential buildup causes a higher negative voltage value after turning the incident light off.

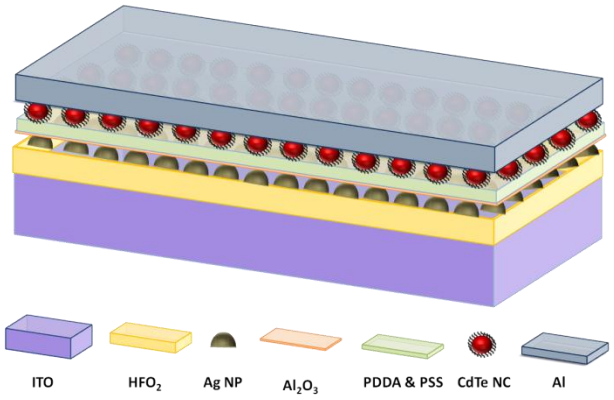

(a)

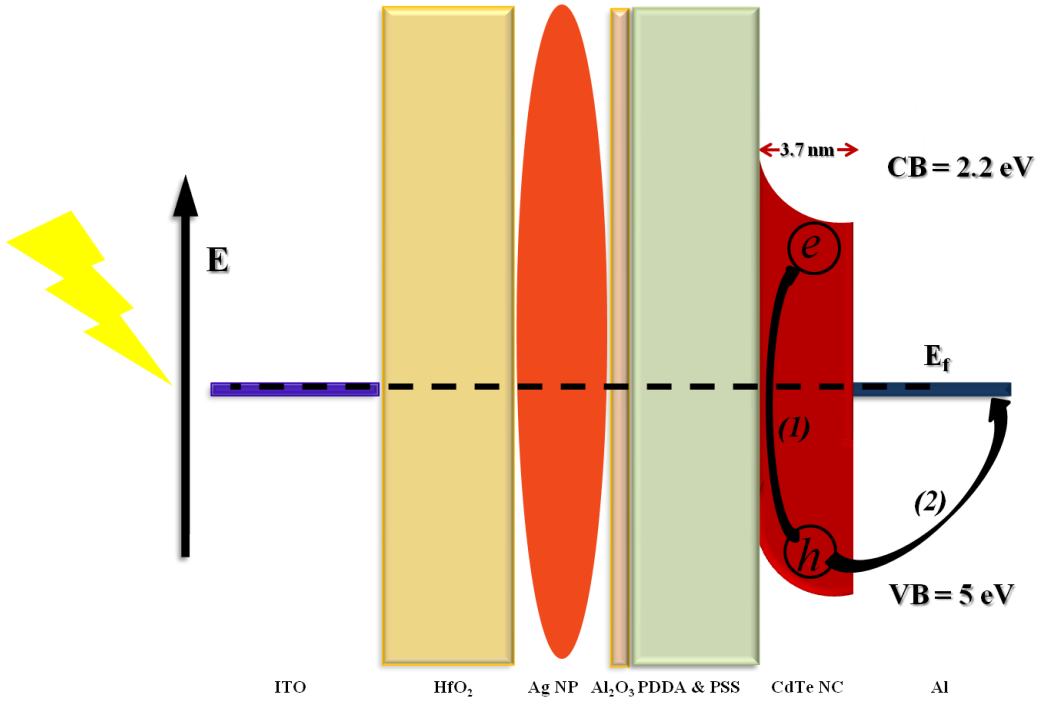

(b)

Figure 5.2.3 (a) Schematic illustration of a plasmonic light-sensitive nanocrystal skin (LS-NS). (b) Surface plasmon resonance sensitization of Ag nanoparticle and band alignment of CdTe NC (3.7 nm in size) conduction band (CB), valence band (VB), and the workfunction (Φ) of Al and ITO. Hence, E_f demonstrates the Fermi level of CdTe NCs at equilibrium condition. After the excitons are photogenerated (1), electrons are remained in the NCs while holes migrate to the Al side (2).

For device fabrication, ITO coated glasses were first cleaned in Hellmanex, Milli-Q water, acetone, and isopropanol in an ultrasonic bath. We then continued by depositing a 50 nm thick HfO_2 dielectric layer via ALD on the ITO substrate. Then, 10 nm silver nanoparticle films were deposited on the dielectric layer at a very low evaporation rate 0.3 Å/s in vacuum environment. Subsequently, the films were annealed using rapid thermal annealing (RTA) at different temperatures and for different durations to modify the LSP resonance peak. In this work we proposed that the enhancement in sensitivity of the LS-NS devices can be promoted by surface plasmon excited in metal nanoparticles and modified density of photon states in NCs at the proper spacing range. In order to make a spacer between NCs and silver nanoparticles, 1 nm Al_2O_3 was deposited

using ALD followed by self-assembly of strong polyelectrolyte poly(diallyldimethylammonium chloride) (PDDA) and poly(sodium 4-styrenesulfonate) (PSS) bilayers via a fully computerized dip-coater system. Since ALD uses pulses of water, it preferentially coats hydrophilic surfaces, which improves the self-assembled film quality [79]. The PDDA and PSS solution is prepared by taking 2 mg/mL in 0.1 M NaCl solution. The PDDA-PSS is self-assembled by sequentially dipping a substrate into the prepared solution for 5 min and rinsed with water for 1 min. The thickness of PDDA-PSS bilayer is approximately 1.4 nm [80] as verified by the optical ellipsometry measurement. After coating one extra layer of positively charged PDDA on top of alternating bilayers of positive and negative polyelectrolyte polymers (PDDA-PSS), negatively charged water soluble CdTe NCs were coated. Substrate was immersed for 20 min using the 4 μM water-soluble CdTe concentration, then it was washed with water for 1 min to remove the extra layers of CdTe NCs [81] to obtain the uniformly coated monolayer of CdTe NCs. Finally, Al contact was deposited using a thermal evaporator on top of the NC layer. As-synthesized CdTe NCs are found to be ~ 3.7 nm in diameter with the first exciton peak at around 605 nm depicted in Figure 5.2.4.

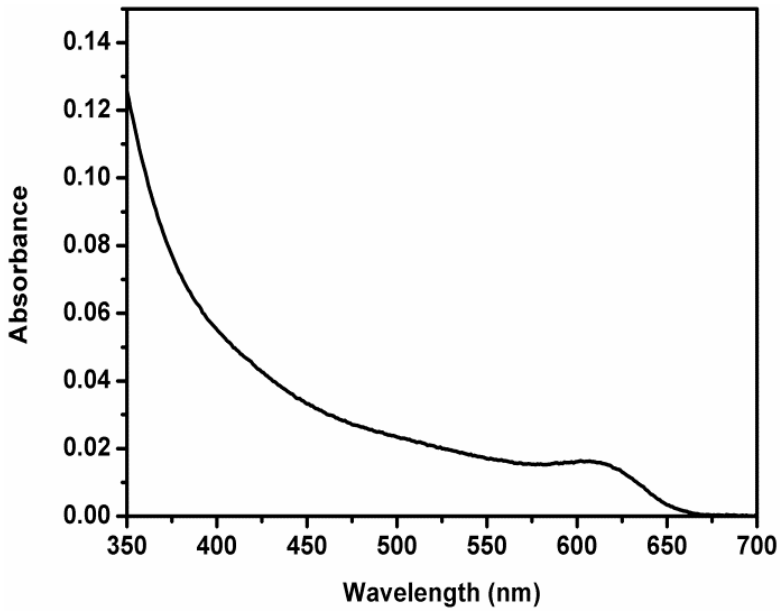

Figure 5.2.4 UV-vis absorption spectrum of aqueous CdTe NCs at room temperature.

All optoelectronic characterizations were performed without applying any electric field using an Agilent Technologies parameter analyzer and a Xenon light source with a monochromator. For the wavelengths longer than 500 nm, a color glass filter (with a cut-off of 400 nm) FSQ-GG 400 Newport was used to prevent the mixing of the second harmonic. Optical power was measured using a Newport 1835C multi-function optical power meter. During the measurements, the sample was connected in series with a load resistance of 200 MΩ with ITO contact grounded.

5. 3 Results and Discussions

The spacing between the plasmonic structures and semiconductor materials affect the enhancement mechanism [82]. Metal enhanced absorption in our structure is based on the interaction between the absorption of the NCs and LSP. In general, the mechanism is based on the influence of NCs absorption close to the metal nanoparticles due to the highly localized electric field in the vicinity of metal nanoparticles. Consequently, the field localization enhances the absorption as long as the spacing between the plasmonic structure and active layer is sufficient to prevent charge accumulation suppression. As a result, we designed our optimal device structure to minimize the effect of suppression and maximize the influence of enhancement. In order to reveal the localized plasmon coupling in the proximity of metallic nanostructures, we separated CdTe NCs and silver nanoparticle by 1 nm thick Al_2O_3 in addition to the bilayers of PDDA and PSS. Aluminum oxide film was set to be only 1 nm thick to have the minimum possible resonance red shift following the assembly of bilayers of PDDA and PSS, and the monolayer of CdTe NCs via dip coating. A varying number of bilayers of PDDA and PSS were deposited on 1 nm Al_2O_3 as an interparticle spacer between metal nanoparticle and semiconductor NCs to investigate the effects of distance dependence of LSP enhancement. Accordingly, we prepared three different sets of devices, each one having its own control sample (bare structure in which there is no plasmonic nanoparticle). The reason for having

individual control sample is the change in the surface coverage of the NCs as the number of polyelectrolyte bilayers changes [83, 84]. Dependence of the absorption on the number of bilayers can directly affect the potential buildup and may enhance photosensitivity of the device. Device sensitivity (S) was calculated by taking the ratio of the voltage buildup (V) and the incident optical power (P) impinging on the device.

The spacing between the plasmonic structure and NCs consists of 1 nm thick Al_2O_3, in addition to varying bilayers of PDDA+PSS and an extra positively charged PDDA layer for depositing negatively charged NCs. We begin with ca. 7 nm spacer consisting of 1 nm Al_2O_3 with 4 bilayers of PDDA+PSS. Comparison of the plasmonic based device structure and the control sample shows the suppression in the voltage buildup and consequently reduced sensitivity of the device. Suppressing the voltage buildup can be explained by the charges trapped inside NCs, which is directly related to the storage of the holes at the Al contact. In the case that the separation distance is not enough or the NCs possibly contact with the metal nanoparticles, electrons are not completely trapped inside the NCs. Instead they can directly migrate to the metal nanoparticles. Consequently, a small amount of charge is trapped inside the NCs, which results in a lower voltage buildup (see Figure 5.3.1(a)). Hence, the control sample has a signal output to yield a voltage buildup around 475 nm; however, the operational wavelength range is limited to 450 nm in the plasmonic structure due to the suppression of charge accumulation. Indeed, for the plasmonic structure beyond 450 nm, the voltage buildup level approaches the minimum noise equivalent intensity; however, this occurs after 475 nm for the control sample (see Figure 5.3.2(a)).

Increasing the spacing between silver nanoparticles and NCs from ca. 7 nm to 11 nm (1 nm Al_2O_3 with 7 bilayers PDDA+PSS) shows a great enhancement. This improvement is basically because of the prevention of the charge accumulation suppression. Consequently, in the presence of metal nanoparticles,

optical absorption of the CdTe NCs film is enhanced, which in turn increases electron and hole generation. When the spacer layer is sufficiently thick to prevent charge accumulation suppression of the NCs, electrons are trapped inside NCs and holes get accumulated at the metal (Al) contact. As a result, a larger voltage buildup can be observed, which consequently enhances the sensitivity of the device (see Figure 5.3.1(b)). We observed up to a 2.6-fold sensitivity enhancement over a broad spectral range (400-525 nm) compared to the control sample. The plasmonic structure exhibits a significant enhancement in the sensitivity at around 525 nm, which also agrees well with the silver nanostructure LSP resonance peak (see the inset of Figure 5.3.2(b)). Furthermore, voltage buildup can be observed at longer wavelengths (up to 650 nm) for the plasmonic device structure compared to the control sample. In other words, at longer wavelengths, due to the low absorption of NCs we observed a higher sensitivity enhancement with the plasmonic structure compared to the control sample. This evidence indicates the absorption enhancement of CdTe NCs via plasmonic silver nanostructures since NCs exhibit low absorption at long wavelengths.

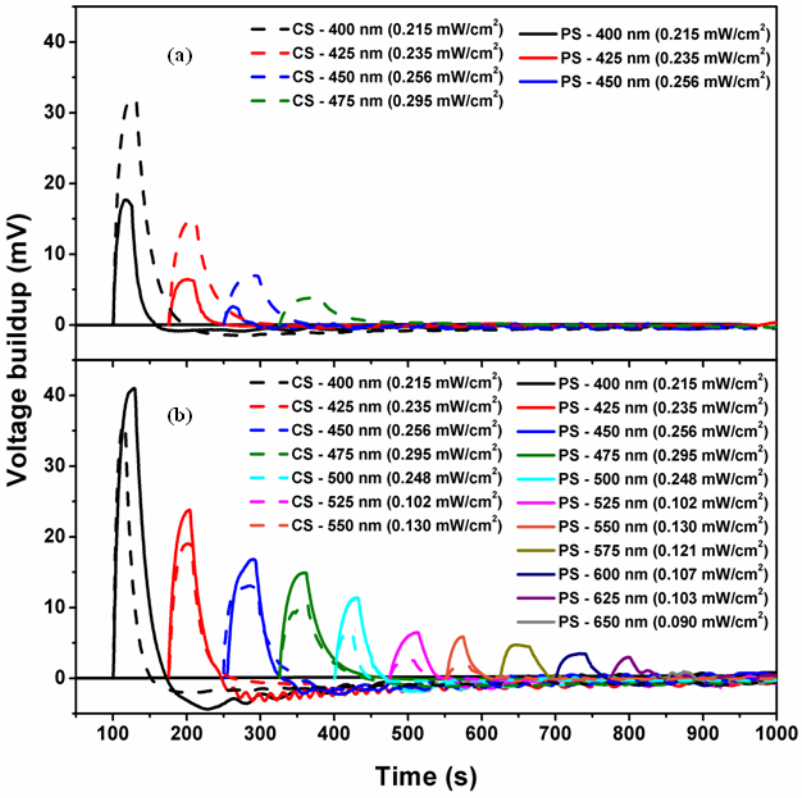

Figure 5.3.1 Voltage buildup variations of LS-NS based on (a) four bilayers of PDDA and PSS and (b) seven bilayers of PDDA and PSS for different excitation wavelengths. Solid line represents the plasmonic sample (PS) and dashed line represents the control sample (CS).

Increasing the interparticle spacer between silver nanoparticle and NCs skin to further ca. 16 nm (1 nm Al_2O_3 with 10 bilayers of PDDA and PSS) to prevent charge accumulation suppression completely enhances the sensitivity and increases the operational wavelength range, though not as much as the 11 nm case. However, a considerable enhancement can still be observed at around 525 nm as a result of LSP of the silver nanostructure (Figure 5.3.2(c)). Moreover, it can be realized that the control sample based on 10 bilayers of PDDA-PSS has a higher sensitivity level compared to the 7 bilayers because of the dependency of the voltage buildup on the number of bilayers. However, the plasmonic structure of 7 bilayers LS-NS is superior to both of the control sample and the plasmonic sample of 10 bilayers in terms of sensitivity around the LSP resonance (see

Figure 5.3.2(b-c)). This is evident in designing plasmonic LS-NS structures that placing a proper separator film between the NCs and plasmonic nanoparticles is one of the important factors that determine the level of plasmonic interactions.

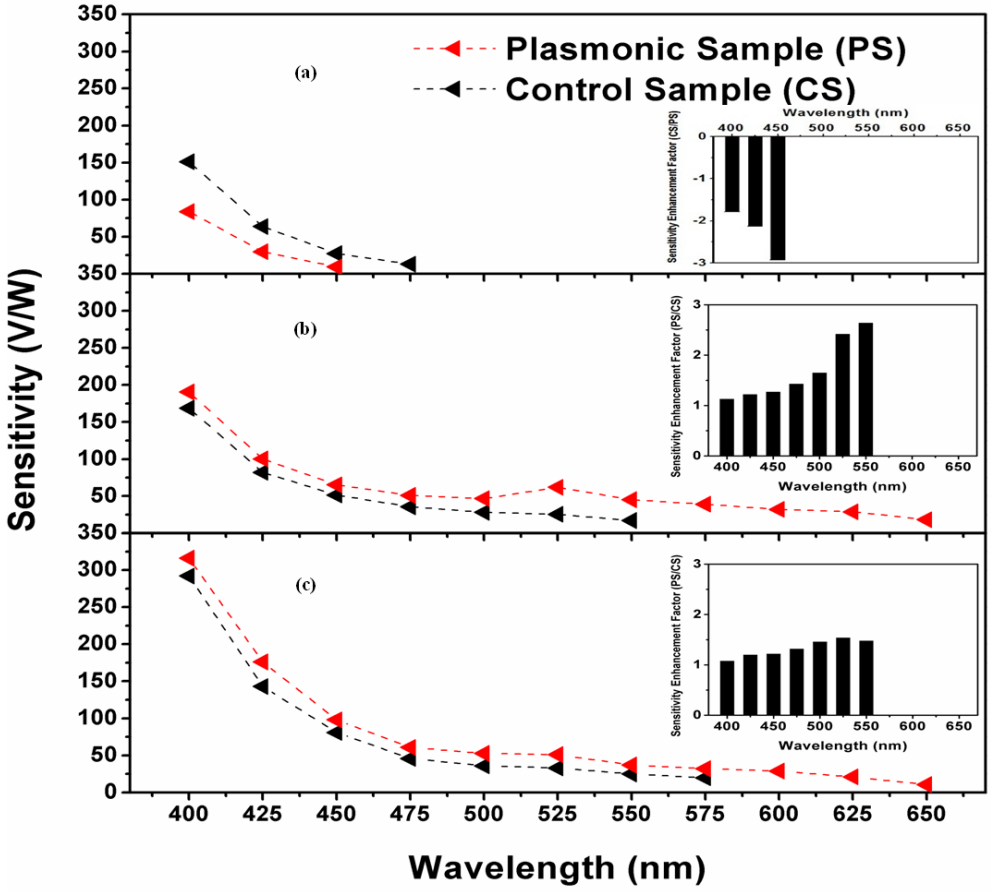

Figure 5.3.2 Comparison of the sensitivity of LS-NS device structure in the absence and presence of plasmonic nanostructures based on (a) four bilayers, (b) seven bilayers, and (c) ten bilayers of PDDA and PSS separating bilayers. Insets Figure presents the sensitivity enhancement factor vs. wavelength.

In order to understand underlying mechanism in sensitivity enhancement of the LS-NS devices, we performed several numerical simulations and observed near field electric field enhancement in the vicinity of the silver nanoparticles. We also compared far field extinction of the simulated nanoparticles with the experimental values. Figure 5.3.3(a) shows the extinction response of the nanoparticles with and without a spacing layer which can be compared to Figure

5.2.2. The difference between the simulation results and the experimental response is attributed to the thickness variation of silver nanoparticles in three dimensions, background noise in SEM image, other smaller particles which are not modeled effectively in this simulation, and limited simulation area compared to real device surface. Subsequently these effects lead to different resonant modes and resonance peak broadening in extinction data. In general, our experimental and theoretical responses look similar.

Cross-sectional electric field intensity maps at special positions shows the electric field intensity localization of the silver nanoparticles at LSP resonance wavelength 520 nm. Figure 5.3.3(b-c) shows the electric field intensity enhancements of HfO_2-Silver nanoparticle interface and spacing layer-air interface, respectively, in the logarithmic scale. Figure 5.3.3(d-e) shows the electric field intensity enhancements of two surface normal cross-sectional maps at random positions indicated with dashed lines in Figure 5.3.3(c). From Figure 5.3.3(c) even at a 11 nm distance from the silver nanoparticles we observe electric field intensity enhancement slightly less than 10 times. The observed locally enhanced electric field due to the resonance of silver nanoparticles supports our assumption that the excitation of the LSP in silver nanoparticles is responsible for the enhancement in the CdTe NCs absorption, which generates more electron-hole pairs.

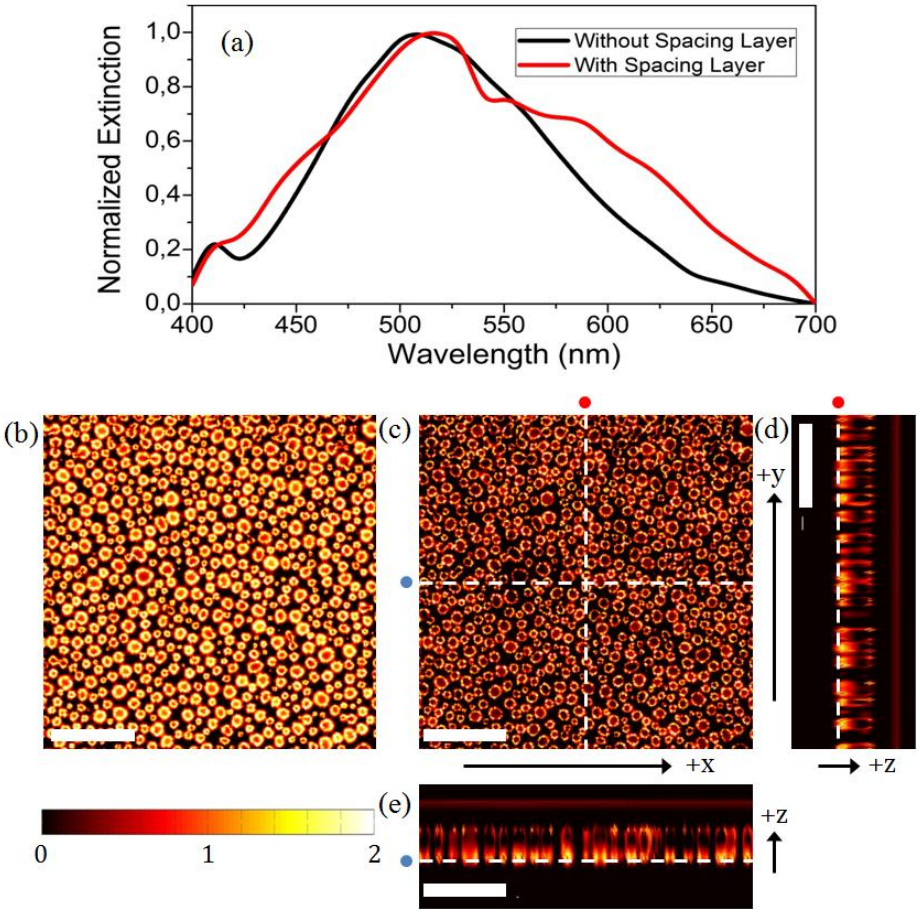

Figure 5.3.3 (a) Normalized extinction of simulated silver nanoparticles with and without spacing layer. (b) Electric field intensity distribution at the interface of HfO_2 film and the silver nanoparticles. (c) Electric field distribution along the interface of the spacing layer and air interface. (d) Cross-sectional 2D electric field intensity distribution along y-z plane. White dashed line coincides with the vertical line of figure 5.3.3(c) indicated with red dots. (e) Cross-sectional 2D electric field intensity distribution along x-z plane. White dashed line coincides with the horizontal line of figure 5.3.3(c) indicated with blue dots. All the color bars and scale bars are identical for the cross-sectional electric field maps. Scale bars correspond to 200 nm and color bar represents relative values of electric field intensity ranging from 0 to 2 in logarithmic scale.

Simulations are run using a commercially available software FDTD solver from Lumerical Inc. The simulated nanostructure was imported from the SEM image in Figure 5.2.1(d) using the import picture property of the software and 20 nm thickness is applied. Then 31 nm dielectric layer encapsulating the silver

nanoparticles is placed giving a 11 nm additional separating layer on top of the silver nanoparticles. 3D simulation region having 800 × 800 nm^2 area with periodic boundary conditions was used since the random distribution of the particles imposes no additional periodicity effect on the plasmonic response. For simplicity, HfO_2 and indium tin oxide (ITO) layers under the silver nanoparticles were taken as simple dielectric layers with an index of refraction of 1.95 and 7 bilayer PDDA + PSS layer was modeled with a dielectric layer having a dielectric constant 1.4. In order to obtain unpolarized response, we performed two simulations with orthogonal source polarizations and, subsequently, electric field intensities and transmission values were obtained using the average value of the results of these two simulations. Based on the simulation results it can be indicated that the experimentally observed well-defined LSP resonance around 525 nm creates localized electric field intensity enhancement at the position of CdTe NCs. Subsequently, this enhancement can generate more electrons and holes in the CdTe NCs.

Chapter 6

Tandem Photosensitive Nanocrystal Skins

6.1 Introduction

From the light detection materials point of view, an ideal photoactive layer material needs to harvest most of the impinging photons in broad spectrum. This would generate a good opportunity for the further improvement of photosensors. Given that the performance efficiency of photosensors is strongly dependent on the fraction of photons absorbed, there is a compromise for the thickness of photoactive layer, which is still a remaining challenge in the electronic properties of NCs solids. Indeed, the active region thickness is restricted in the order of or considerably less than, 100 nm due to the relatively short minority carrier diffusion length. To increase absorbance, increasing film thickness is not a good approach since it may exceed the diffusion length. Similarly, thickness limitation reduces the device transparency and influences the noise generation-recombination. Furthermore, the use of a thin film based photoactive layer is effective for avoiding the self-absorption effect. In conventional photosensors to collect the photogenerated carriers external bias need to be applied, which sometimes influences the photoactive layers and degradates the NC film. Furthermore, increasing illumination leads to the saturation of deeper and

shallower trap states, which results in acceleration of the response time but at the expense of having a reduced sensitivity.

In this work, we present a new device design structure to overcome the aforementioned challenges for solution processed light-sensitive devices. Here highly sensitive tandem photosensitive NC skins (PNS) are achieved by spray coating a single monolayer of UV-VIS CdTe NCs on top of the substrates that operate without any external bias. Usage of single monolayer NCs and few nanometers aluminum as the electrode, a semi-transparent tandem PNS was obtained. In this type of devices, higher sensitivity can be obtained if the absorption of the photoactive layer is increased. When we adapted a thick photoactive NCs layer, a much lower photovoltage buildup was observed which was attributed to the self-absorption effect. Consequently, because of the principle operation dependency of the device on the single monolayer NCs, we have successfully developed a tandem PNS composed of two constituent junctions, each consisting of a single NC monolayer. Usage of single monolayers of NCs as the photoactive layer significantly reduces the noise generation and recombination.

6.2 Results and Discussions

To fabricate the devices, we used ITO coated glass. As shown in Figure 6.2. 1(a), the semi-transparent tandem PNS configuration was glass/indium tin oxide (ITO)/ (hafnium dioxide) HfO_2/ poly(diallyldimethylammonium chloride) PDDA & poly(sodium 4-styrenesulfonate) PSS/ CdTe NCs/ Al/ HfO_2/ PDDA-PSS/ CdTe NCs/ Al. The monolayers of UV-VIS light-sensitive CdTe NCs are sandwiched between transparent polyelectrolyte polymers and semi-transparent Al electrodes. Figure 6.2.1(b) shows the film absorption of the photoactive layer consisting of a single monolayer of CdTe NCs with the absorption located below 650 nm.

These NCs are capped with TGA ligand to stabilize their dispersions. However, these ligands are insulating and prevent charge transport through NCs in solid state at the same time. We have already shown that NCs eradicated from ligands can be coated to form uniform, crack free, randomly close packed NC thin film. This greatly expands the applicability of these materials compared with the presence of ligands. Regarding a higher absorption coefficient of CdHgTe (6 nm in size) NCs, CdTe (3.4 nm in size) NCs were preferred for the bottom junction since it is more efficient to accumulate the photogenerated charges from smaller NCs compared to the bigger one. Indeed, we observed that in big NCs surface trap states are more probable which prevents the charges migration to the electrode.

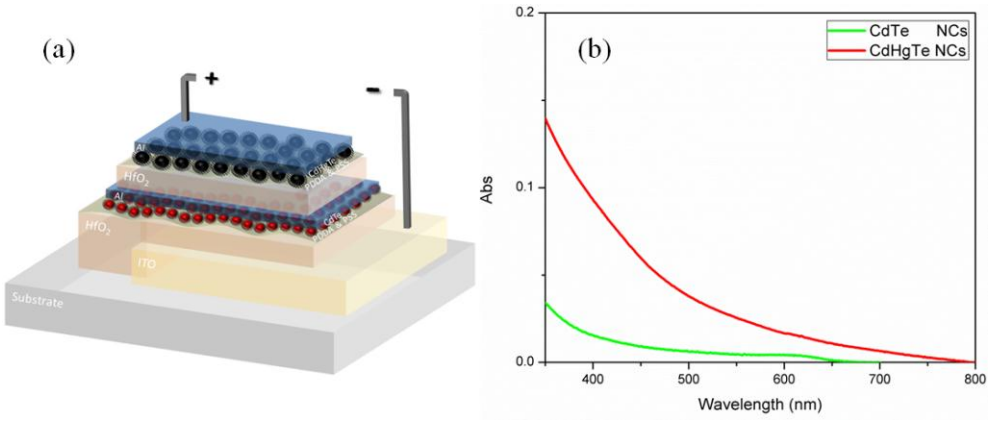

Figure 6.2.1 (a) Schematic of the device architecture for solution-processed semi-transparent tandem photosensitive nanocrystal skins. (b) Absorption spectra of single colloidal CdTe and CdHgTe NCs monolayers.

To ensure the transmission of light, for both the electrodes on top of the NCs we deposited only 10 nm thick Al via thermal evaporator under vacuum condition. The tandem PNS showed >10% optical-transparency in the wavelength range of 350-800 nm. Moreover, the 10 nm Al layer was evaporated immediately onto the NCs monolayers serving both as the electrode layer and as a protective layer to protect the NCs from exposure to reactive oxygen. Because of the energy band diagram of NCs and Al, the presence of NCs as the photoactive layer underneath the electrode helps to avoid the need for any external bias to

dissociate the photogenerated excitons. Hence, the absence of any energetic barrier at the interface of NCs and Al electrode allows for the photogenerated holes immediately to migrate to the aluminum, resulting in higher sensitivity. Moreover, independency of the device on the external bias, boost the stability of the device and diminishes the effects for the NCs film degradation.

ITO coated atop a glass substrate was chosen as the bottom electrode. The substrate was exposed to oxygen plasma to create additional hydroxyl groups necessary for the ALD of HfO_2 high dielectric constant layer. The great challenge in fabricating the tandem PNS is to deposit thin enough dielectric spacer layer on top of the large area ITO in order to prevent any charges migrating from the NCs to the ITO. We intentionally deposited 50 nm HfO_2 via ALD at a low temperate of 80 ˚C temperate to prevent any catastrophic damage to the NCs since they were synthesized in the boiling water at 100 ˚C. ALD preferentially coats hydrophilic surfaces owing to the usage of pulses of water, which improves the self-assembled film quality. Moreover, the encapsulation with HfO_2 averts any crack damage to the substrate in the further fabrication steps. After that, oppositely charged PDDA and PSS bilayers were coated via a fully computerized dip-coater system. The other challenge was the monolayer coating of the NCs on top of the large area polyelectrolyte polymers. To solve this problem, a spray-coated NC-based solution was applied in our approach to achieve the transparent monolayer photoactive layer. Spray-coating of NCs gives us the opportunity to cover a small amount of NCs over large areas. The NCs coated substrate was then washed under water to ensure that extra NCs were removed.

The proposed platform demonstrates higher sensitivity if we manage to increase the number of photogenerated electron-hole pairs. Subsequently, we proposed an extra monolayer of NCs to be integrated inside the device in order to increase the photogenerated potential buildup. Since during the device operation we do not apply any external bias, exactly below the aluminum electrode, we need to

have only a single monolayer of colloidal NCs. Subsequently, we add an extra junction to the conventional CdTe based light-sensitive device. With the addition of constituent junction of CdTe monolayer, we demonstrated that sensitivity of the PNS devices increases significantly.

Using our tandem PNS, we verified our concept of enhancement in sensitivity as mentioned above. Figure 6.2.2 shows the photoresponse spectra of the tandem structure under the incident light. In response to the excitation wavelength and illumination intensity we observed a higher voltage buildup at shorter wavelengths. Similarly, as a result of increased optical absorption at shorter excitation wavelengths, which increases the number of trapped electrons inside the NCs, we observed a higher negative voltage after switching off the light. As a result of increased charging of the NCs by the trapped electrons at shorter excitation wavelengths, it takes more time to recover after the light exposure is switched off. The photodetection sensitivity of the PNS was defined as the ratio of photovoltage buildup (V) to the impinging optical power (P) on the device. We constructed two classes of control devices to eludicate the benefits of the tandem PNS. The performance of control devices is depicted in Figure 6.2.2. In the testing of the control samples, we measured their performance with illumination from the top side to coincide with the tandem PNS, which shows the best performance from the top.

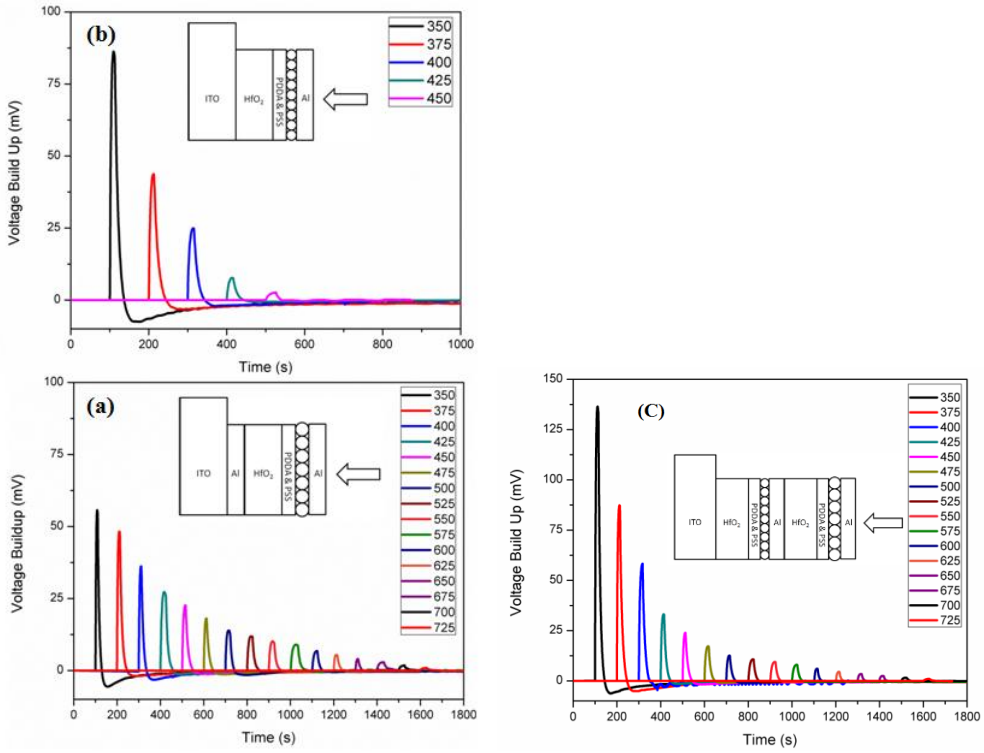

Figure 6.2.2 Photovoltage buildup at different excitation wavelength and optical intensity levels for devices based on (a) CdTe and (b) CdHgTe, and (c) the device using both CdTe and CdHgTe.

To compare the tandem and single junction PNS, all measurements from the samples were taken under the same condition. The ideal tandem PNS should exhibit a photovoltage buildup equal to the sum of the photogenerated potential buildup of the constituent junctions. The PNS device achieves a total photovoltage buildup at each wavelength, equal to within few percent to the sum of the photovoltage buildup of the individual single junctions. We attribute this small difference to the mismatch between the interface layers in the tandem PNS. To understand the reproducibility of the results obtained, over 40 samples were prepared in developing the fabrication process, with the best performing device reported here. In the conventional NC-based photodetectors, impinging higher intensity light on the device is followed by the occupation and saturation of deeper and shallower electron trap states in the NCs. This accelerates the response time but at the expense of reduced sensitivity. Such a compromise

would curtail photovoltage buildup, leading to a significantly reduced sensitivity.

The benefit of introducing a tandem PNS is twofold. It is expected to observe the response time to be accelerated when we adapt the two separated junctions incorporated into one structure. Since each one behaves like a capacitor, by fabricating two of them on top of each other; the capacitances are connected in series. As a result, the total capacitance decreases, which speed up the RC decay response time. Furthermore, on the contrary to the conventional multijunction devices, for which the current matching between the junctions is essential, there is no such limitation in tandem PNS devices. The photogenerated holes from an adjacent monolayer are accumulated at the top electrode, contributing its potential buildup to the overall device response. It should be noted, however, that the detection sensitivity remains small in the long wavelength region where NCs exhibit low optical absorption. Essentially, this is because there are fewer electron and hole states available in a NC at lower photon energy. This behavior indicates the wavelength dependency of the PNS and is in strong agreement with the profile of optical absorption spectrum of CdHgTe and CdTe NCs. Moreover, any probable cavity effect from the two Al electrode in the tandem PNS was investigated. We designed the layers constituting the tandem PNS to be as thin as possible to minimize any cavity effect to prevent any complexity in studying kinetics of the device. However, this can be also used to benefit from resonant cavity enhanced absorption with a proper design.

Chapter 7

Nanocrystal Skins With Exciton Funneling For Photosensing

7.1 Introduction

With a single NC layer in the device structure, noise generation is significantly reduced, which enhances the device sensitivity. However, in this case, limiting these devices to a single NC layer for absorbing incident light hinders performance. In operation, with exciton disassociation due to the difference between the work functions of the NCs and the metal contact, electrons are trapped inside the NCs and holes are accumulated in the metal electrode, leading to a potential buildup across the device. Thus, although increasing the NC layer's thickness results in increased optical absorption, in the absence of any applied bias across the device, photogenerated excitons may not disassociate and sufficient charge may not accumulate. Thus, photosensitive NC skin performance depends not only on the optical absorption but also on the capacity to accumulate dissociated excitons.

For the above reasons, we posit that by relying on the direct relationship between increasing the number of trapped electrons inside the NCs and subsequently the accumulated holes in the metal contact, a larger potential buildup in the photosensitive NCs skins will occur. We therefore pursue a

cascaded structure of semiconductor NCs with the necessary band gap gradient to enable exciton funneling expecting a considerable improvement in the sensitivity. We fabricate photosensitive NC skins based on the Schottky barrier at the interface between the top CdTe NCs and Al contact (Figure 7.1.1(a)). A thin film of transparent indium tin oxide (ITO) underneath a dielectric film forms the opposite contact. Due to the device architecture and full surface coverage of the current blocking dielectric film made of 100 nm hafnium oxide (HfO_2) and four bilayers of polydiallyldimethylammonium chloride-polysodium 4-styrenesulfonate (PDDA-PSS), the photosensitive NC skin itself acts as a capacitor.

Figure 7.1.1(a) shows a schematic drawing of the closely packed NC monolayers. Because of the considerable change in the NC surface coverage as the number of polyelectrolyte bilayers changes, we found that four bilayers of PDDA-PSS were necessary to provide a uniform film with enough surface coverage for depositing the CdTe NC monolayer. Light incident through the glass substrate generates excitons in the NC monolayers. The excitons funnel along the gradually decreasing band gap gradient of cascaded NC monolayers, and are finally captured by the NC monolayer with the largest band gap adjacent to Al contact, which acts as a hole acceptor. These excitons are then dissociated at the NC-Al interface, and thus, holes migrate to the Al contact due to the HOMO/LUMO band alignment of the NC layer and the Al workfunction, as shown Figure 7.1.1(b). Electrons, however, remain trapped inside the NCs.

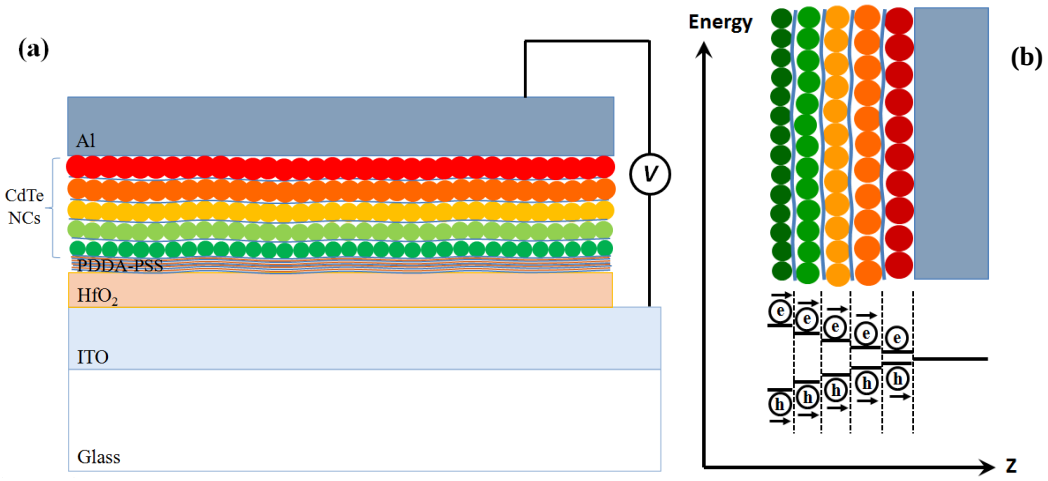

Figure 7.1.1 (a) Schematic of the photosensitive NC skins, consisting of closely packed layers of ligand-free CdTe NCs. (b) Alignment of the conduction and valence bands of the CdTe NC layers and the workfunction of the Al contact. Excitons transfer through the layers from smaller to larger NCs because of the band gap gradient.

Controlling NC surface passivation is critical for efficient device operation, and because no external bias is applied through our cascaded NC structure, efficient exciton transfer must be achieved through some other method. NCs are normally separated from each other via ligands of isolating organic molecules that passivate NC surfaces through oxidation and chemical modifications. The ligands also control electronic NC properties including conductivity and charge mobility. To bring NCs closer, we removed the ligands by adding isopropanol to the CdTe NC solution and centrifuging the mixture.

For this work, we synthesized water-soluble CdTe NC-capped TGA ligands of different sizes and calculated the NC diameters from their extinction spectra. These diameters were 2.90, 2.98, 3.19, 3.62, and 3.71 nm, leading to the first excitonic peak wavelengths of 525, 532, 545, 595, and 605 nm, respectively.

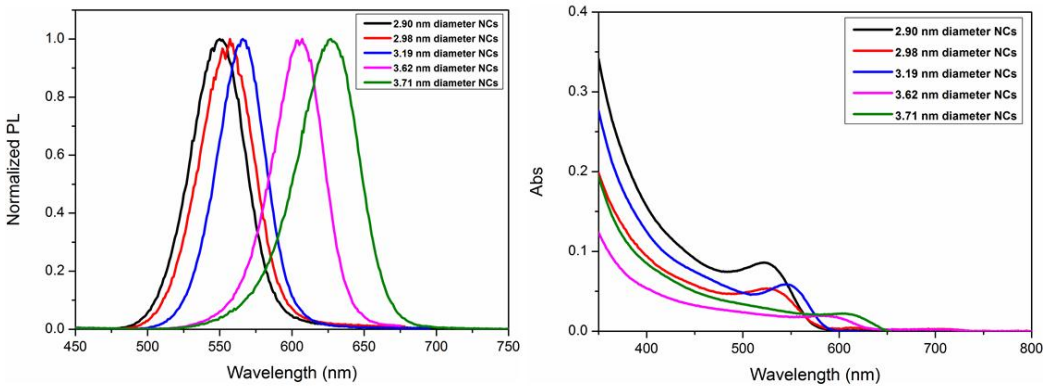

Figure 7.1.2 Photoluminescence and UV-vis absorption spectra of as-synthesized aqueous CdTe NC solutions at room temperature.

7. 2 Results and Discussions

In this work we demonstrate that with the proper energy gradient of NC skins composed of several monolayers, photosensitivity can be substantially enhanced and extremely broadband photosensitivity can be achieved. Figure 7.2.1 shows the photovoltage buildup as a function of time across four devices that we fabricated. For the device utilizing a single NC layer as the photoactive layer, we show that varying photovoltage buildup amounts at different excitation wavelengths, Figure 7.2.1(a). Increasing the number of the same NC layers from one to five leads to greatly enhanced absorption, but we observe voltage buildup suppression and a consequent reduced level of the device sensitivity compared to the single layer. Voltage buildup suppression can be explained by the self-absorption effect in the lowermost NC layers; fewer fractions of photons reach the topmost NC layers and excitons photogenerated in the bottom NC layers cannot make it to the top which leads to fewer electrons and holes being trapped in the NCs and stored at the Al contact. Additionally, in the absence of a band gap gradient, each exciton tends to remain in the layer where it was created until it is recombined. Therefore, given that the device performance efficiency is strongly dependent on the fraction of photons absorbed, a balance must be found

between the thickness of the photoactive layer and the thicknesses of the NC layers.

Previously, Franzl et al. proposed that NC funnel-like band gap profiles transfer excitons to the largest NCs with the smallest band gap. The funnel structure recycles the trapped and lost electron-hole pairs, leading to enhanced photoluminescence (PL) of the largest NCs as well [85]. In this work, we focus on three structures composed of five NC monolayers, where the NC sizes differ depending on the structure (see Figure 7.2.1(b-d)). The band gaps of the CdTe NCs are adjusted to transfer photogenerated excitons from the layers comprising smaller NCs to the layer comprising the largest NCs, which is immediately underneath the Al contact. Compared to the device with a single NC layer, the device with multiple NC layers placed within the proper band gap gradient exhibits a significant enhancement in the sensitivity and a considerable extension in the operating wavelength range (see Figure 7.2.1(a-d)).

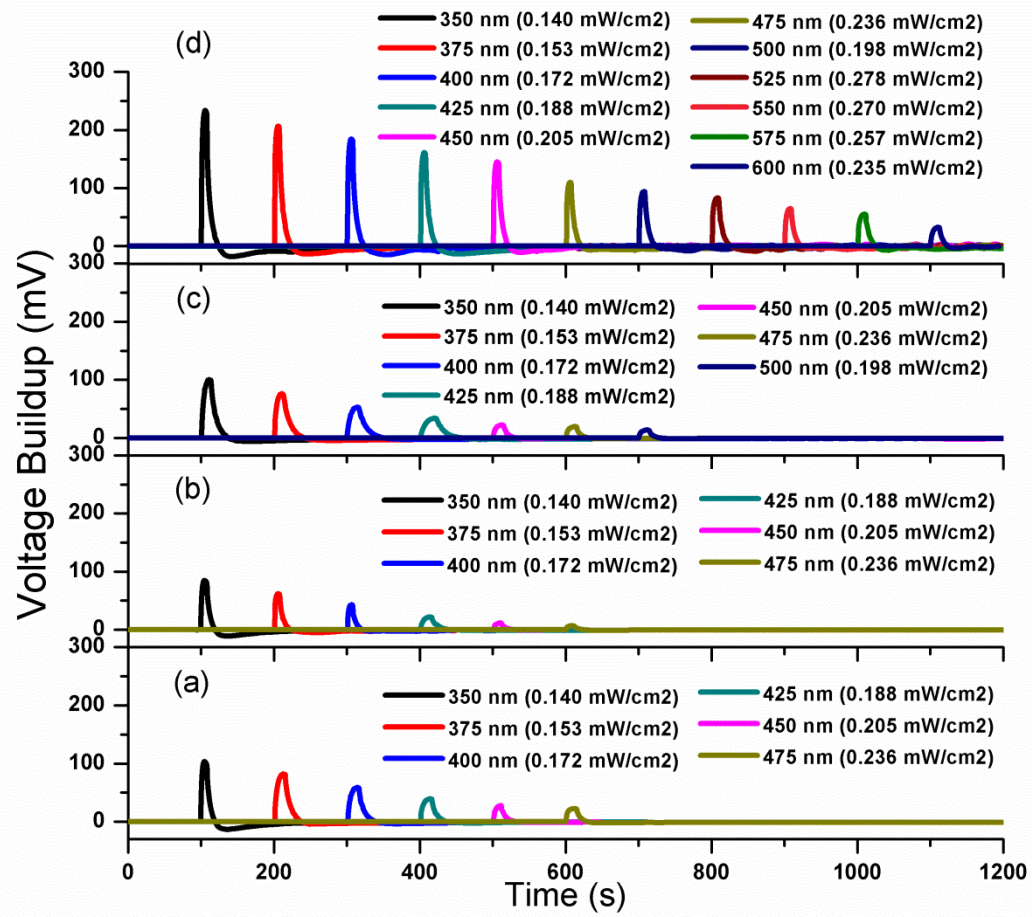

Figure 7.2.1 Experimental photovoltage buildup results of photosensitive NC skins at different excitation wavelengths and intensity levels based on (a) a single layer of NCs, (b) five layers of NCs of the identical size, (c) five layers of NCs ranging from large to small, and (d) five layers of NCs ranging from small to large.

The observed enhancement in the proposed cascaded structure's voltage buildup behavior can be attributed to the excitonic transfer from the smallest NCs to the largest NCs. After the excitons reach the largest NC layer, the excitons dissociate and the holes migrate and accumulate at the Al contact. Similarly, the electrons are trapped inside the NCs, as observed from the negative voltage levels of the photovoltage spectrum (Figure 7.2.1).

As evident from Figure 7.2.1(d), we achieve a more than twofold enhancement in photovoltage buildup in the multilayer device compared to the monolayer

device. Furthermore, the cascaded NC skin structure exhibits considerably improved spectral behavior, with its operating wavelength range between 350 and 600 nm.

To investigate the effect of the band gap gradient in a funnel-like device, we study the order dependence of NC layers by fabricating a converse structure (accumulating photogenerated excitons from layers with smaller NCs to layers with larger NCs, now placed far away from the Al contact), whose voltage buildup is presented in Figure 7.2.1(c). The low performance of the converse funnel-like device is attributed to the depopulation of photogenerated excitons from the layers with smaller NCs because of the energy gradient in the reverse direction. Thus, fewer numbers of holes accumulate at the Al contact and consequently, fewer electrons become trapped in the NC layer under the Al contact. This observation strongly coincides with the proposed excitonic transfer process of NC exciton population and depopulation dynamics via nonradiative energy transfer toward the layer with the largest NCs.

As can be seen from Figure 7.2.1(c-d) the response time of the converse funnel-like device is slower than the gradient device with the ideal band gap. This result indicates that, although the excitons become disassociated in the former device, due to the unfavorable band gap gradient, they separate from the Al contact and remain longer in the device, which results in a slower operation.

We calculated NC skin photosensitivity according to the ratio of $S = V/P$, where V and P are the photovoltage buildup and incident optical power impinging on the device, respectively. Figure 7.2.2 demonstrates the corresponding sensitivity curves as a function of the excitation wavelength. Similar to the observed photovoltage buildup behavior, the sensitivity spectra also follow the NC absorption spectrum and increase as the photon energy increases.

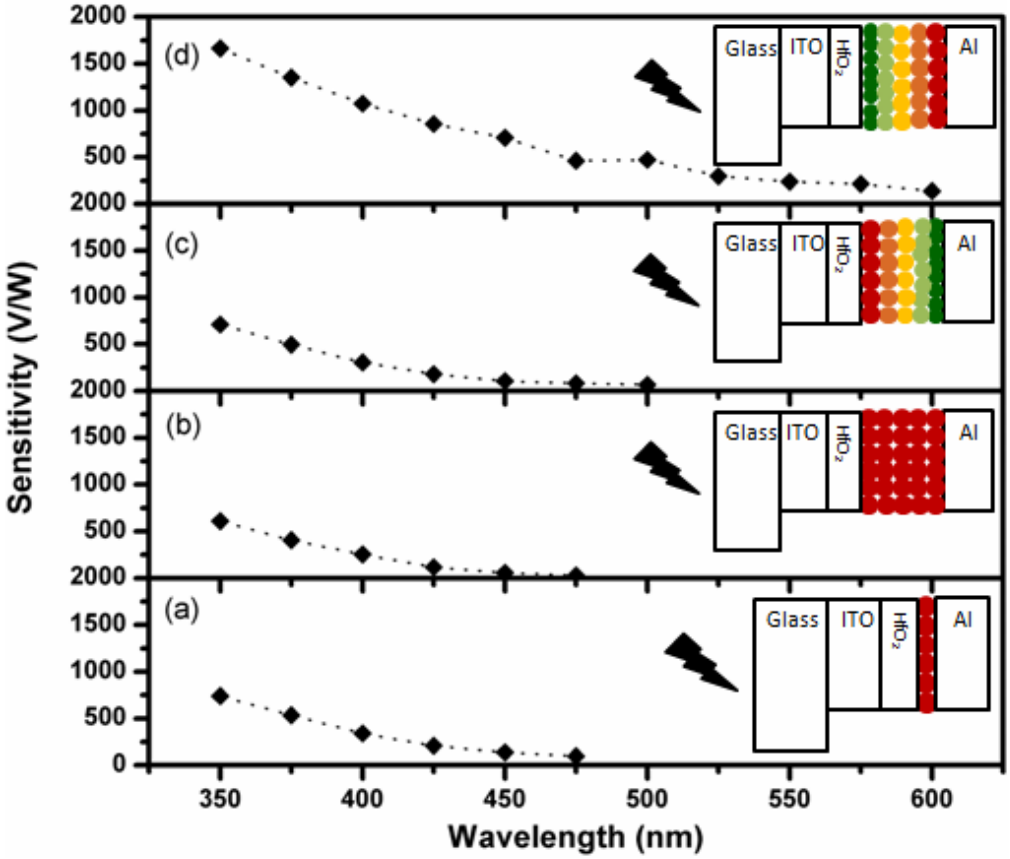

Figure 7.2.2 A comparison of the corresponding sensitivities as a function of excitation wavelength based on (a) a single layer of NCs, (b) five layers of NCs of the identical size, (c) five layers of NCs ranging from large to small, and (d) five layers of NCs ranging from small to large. Inset figures present the device schematics and the direction of incident light.

The absorption and emission spectra of the distinct sizes of the CdTe NCs show considerable overlap; therefore, as the physical basis for exciton transfer, nonradiative exciton transfer (NRET) from small NCs to large NCs can be considered to be a very likely process [86]. To further verify the presence of NRET between these NC layers, we conducted time-correlated single-photon counting experiments (Picoquant, Fluotime 200) with a calibrated time resolution of 32 ps and a pulsed excitation laser diode at 375 nm. We conducted time-resolved fluorescence (TRF) measurements of the cascaded NC structure at the emission peaks of the smallest (donor-side) and largest (acceptor-side) NCs,

which were 545 and 645 nm, respectively. These peak wavelengths correspond to the respective emission peaks of the dark green layer (smallest NCs) and the red layer (largest NCs). The dynamics obtained in the experiments include the fluorescence decays of the NCs convolved with the system instrument response function (IRF). When analyzing the TRF results, we used multiexponential least chi-square fittings in the reconvolution mode to determine the system's IRF Picoquant Fluofit.

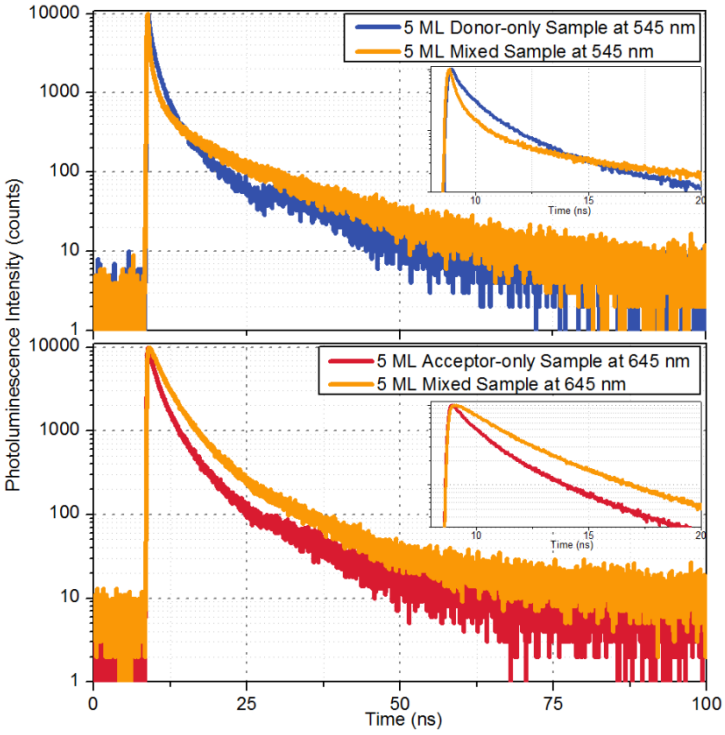

Figure 7.2.3 Time-resolved PL decays of the five donor NC layer samples, the five acceptor NC layer samples, and the five hybrid-layer samples. Insets show the first 20 ns parts of the decays.

To verify the existence of NRET, we conducted experiments on five monolayers of donor-only NCs, acceptor-only NCs, and cascaded samples with the band gap gradient. As evident from Figure 7.2.3, there is a clear difference between the TRF decays of the donor-only sample and the hybrid sample for the measurements at 545 nm, the PL peak of the donor NCs. The amplitude-

averaged donor lifetime becomes 0.304 ns in the hybrid sample and 0.567 ns for the donor-only sample, which is a clear indicator for the presence of the NRET process from the layer with the smallest NCs to the four layers with larger NCs. To verify exciton feeding to the layer with the largest NCs (acceptor NCs) from the four layers with the smaller NCs, we took TRF measurements of the acceptor-only sample and the hybrid sample at the emission peak (645 nm) of the red (largest) NCs. The acceptor-side average lifetime of the hybrid sample was 2.86 ns, whereas the acceptor-only sample lifetime was 1.66 ns. These significant decay lifetime differences are shown in Figure 7.2.3, and the PL spectra are shown in the Figure 7.2.4. These observations indicate that NRET occurs between the NC layers, and therefore, we can attribute the enhancement in photovoltage buildup and the consequent sensitivity improvement to NRET towards the top NC layer with the desirable energy gradient of the NC films.

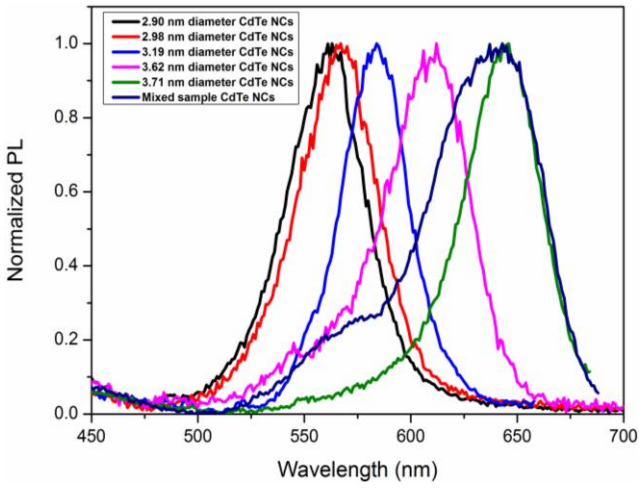

Figure 7.2.4 Normalized photoluminescence spectra of five NC monolayers of different sizes on the glass.

Although the NRET from the small NCs to the large ones is evident, its efficiency could in principle be higher. The ligand removal process may cause new nonradiative decay channels in the NCs, thus resulting in very fast NC decay; hence, NRET may become less effective. It is important to note that the

monolayer-based device can build up approximately 100 mV under 0.170 mW/cm^2 at 350 nm. The cascaded monolayer device in the proper funnel structure was thus expected to show a photovoltage buildup of about 500 mV under similar experimental conditions, but the observed voltage buildup was only about 245 mV in all our fabricated funnel-based devices. This deficiency in performance indicates that exciton transfer in the funnel structure is not fully efficient. Excitons can be trapped between NC layers because of intervening polyelectrolyte layers, surface states, and defects created in the layer-by-layer assembly, and we surmise that such events occurred in these experiments.

Chapter 8

Photosensitivity Enhancement in Semi-transparent Light-sensitive Skins of Nanocrystal Monolayers with Electron Transfer to TiO_2

8.1 Introduction

In the first generation of NC light-sensitive skins, NCs closely interact with the top interfacing contact while the other side is isolated using a high dielectric constant spacing layer. After excitons are photogenerated, electron-hole pairs are dissociated at the aluminum (Al) and NC monolayer interface. Owing to the Al workfunction and band alignment of the NC monolayer, holes migrate and accumulate at the Al side, which serves as hole acceptor. On the other hand, because of the dielectric layer of hafnium dioxide (HfO_2) electrons remain inside the NCs. In these devices, the more the electrons and holes are photogenerated, the higher voltage buildup can be obtained. Nominally, electrons and holes tend to recombine in the NCs. Therefore, there is a competition between exciton diassociation and exciton recombination. Consequently, we posit that, by further separation of the holes and electrons to decrease the recombination probability within the device, a favorable enhancement in the device performance can be obtained by transferring

electrons from NCs to an electron acceptor layer. The higher conduction band level of NCs can serve as the driving force for electron injection from the NCs to nearly acceptor with a lower conduction band level. Subsequently, we propose that in light-sensitive skins favorable conduction band offset may aid in transferring the electrons from NCs to the electron accepting material TiO_2. Hence, majority of the holes migrate towards the top Al contact. The schematic band diagram of the TiO_2 and Al, which serve as the acceptors for the electron and the hole, respectively, is shown in Figure 8.1.1(a). In this work, we employed TiO_2 layer that was engineered to transfer electrons from CdTe NCs to decrease the recombination probability of the photogenerated excitons in the NCs. This segregation leads to increased sensitivity of the LS-NS devices. Therefore, integrating the monolayer NC film with a TiO_2 layer offers a great potential for large-area photosensitive windows and glass facades of smart buildings.

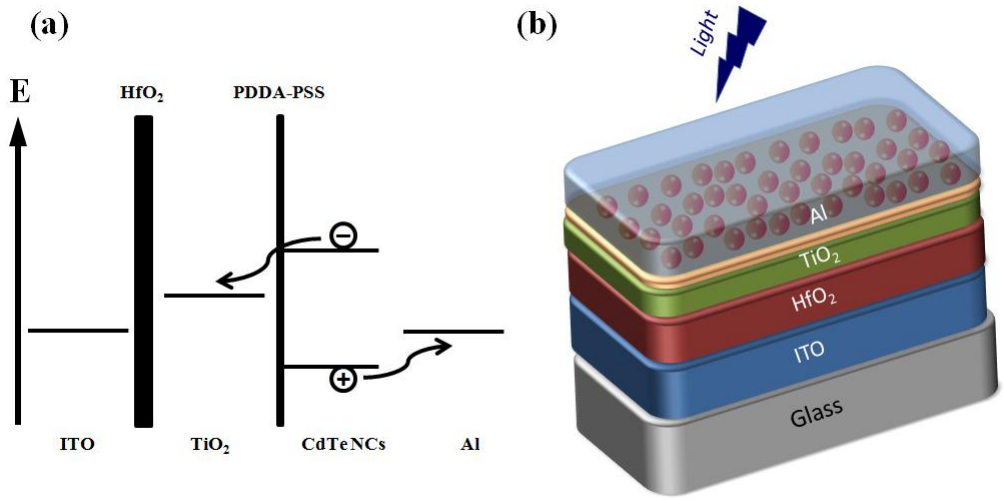

Figure 8.1.1 (a) Energy band diagram and (b) schematic of the LS-NS device incorporating TiO_2 layer.

8.2 Experiments

We fabricated light-sensitive skins using both TiO_2 deposited sample and the reference sample without any TiO_2 layer. In a quest to find a proper electron

accepting material, Jin et al. reported the process of electron transfer (ET) from NCs to TiO_2 layer grown by ALD [87]. In addition, ALD uses pulses of water, which preferentially coats hydrophilic surfaces and improves the quality of self-assembled films. UV-visible absorption spectra showed that TiO_2 has absorption in the spectral region from 350-600 nm, shown in Figure 8.2.1.

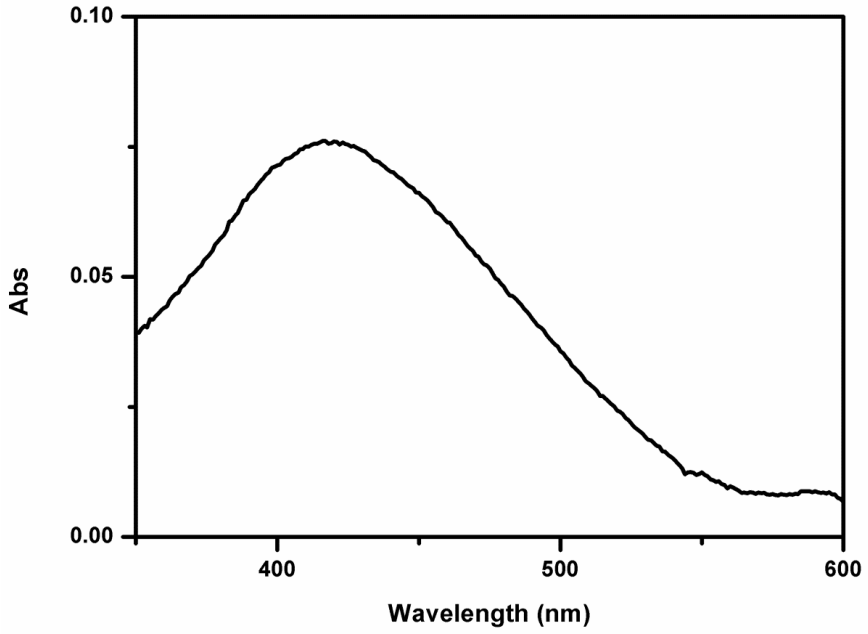

Figure 8.2.1 Absorption spectrum of 10 nm TiO_2 on HfO_2 coated glass.

The average diameter of as-synthesized CdTe NCs was found to be 3.7 nm with the first excitonic peak at around 605 nm and the photoluminescence emission at about 627 nm (Figure 8.2.2). Furthermore, we note that another means of decreasing the recombination probability of photogenerated electrons and holes in these devices relies on surface passivation of the NCs. Indeed, charges encounter high potential barriers due to the ligands passivating the NCs surface. To enhance the electron transport and charge conductivity, we partially removed the TGA ligands from the NC surfaces by adding isopropanol into the CdTe NC solution and centrifuging the mixture. During the film assembly, NC solution was rigorously stirred to prevent any precipitation.

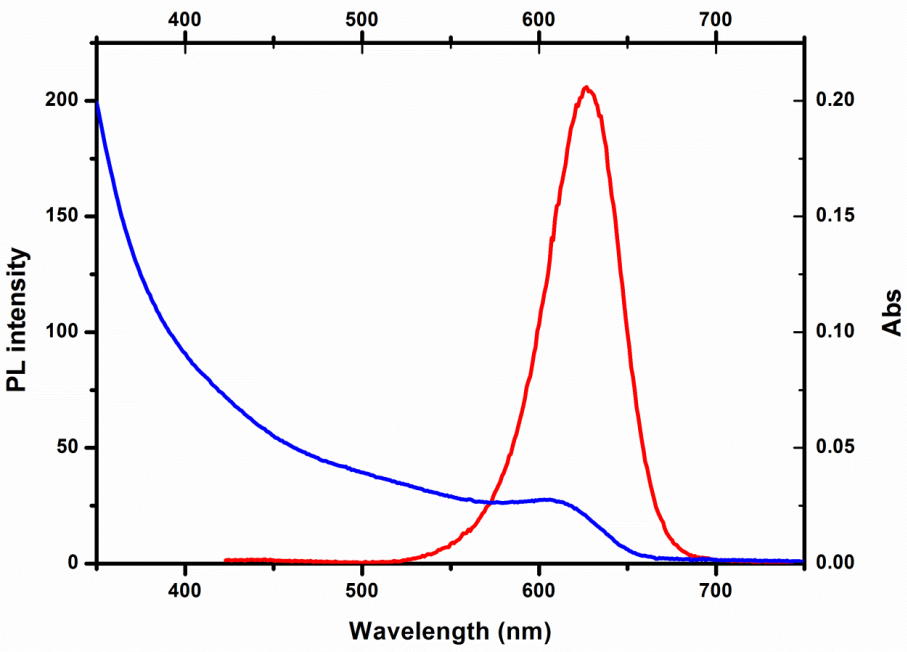

Figure 8.2.2 Photoluminescence and UV-vis absorption spectra of as-synthesized aqueous CdTe NCs in solution at room temperature.

For the device implementation, after cleaning the ITO film deposited on glass substrate, a 50 nm thick HfO_2 dielectric film, followed by 10 nm TiO_2, was deposited using ALD (Savannah) at 150 ^{o}C. Subsequently, to deposit the NCs, we used layer-by-layer self-assembly via computerized dip coating system. Negatively charged CdTe NCs were coated on top of the bilayers of PDDA-PSS serving as strong polyelectrolyte polymers. Finally, a semi-transparent, very thin, Al contact was deposited on top of the NC layer using a thermal evaporator. The device architecture for the light-sensitive skins with an electron accepting layer (TiO_2) is depicted in Figure 8.1.1(b).

We carried out all optoelectronic characterizations at room temperature and no external bias was applied across the device. Voltage buildup vs. time characteristics was measured using an Agilent Technologies parameter analyzer and a Xenon light source with a monochromator. In operation, the devices were connected to a 200 MΩ shunt resistor, with the ITO contact grounded. Optical power was measured using a Newport 1835C multi-function optical power

meter. Due to the slight absorption of TiO_2 layer, all devices were illuminated from the top (Al) side.

8.3 Results and Discussions

For a detailed understanding of the effects of TiO_2 layer incorporation in light-sensitive skins on the device operation and performance, we systematically vary the excitation wavelength and illumination intensity. Voltage buildup vs. time characteristics for the devices based on four bilayers of polyelectrolyte polymers (PDDA-PSS) under the Xenon light source with the monochromator is shown in Figure 8.3.1(a-b). We observed higher voltage buildup as the excitation wavelength is shortened, followed by a larger negative voltage value after switching off the light. This is due to the stronger optical absorption of CdTe NCs at shorter optical wavelengths. At higher photon energies, NC can absorb larger number of photons, photogenerating more electrons and holes compared to longer wavelength excitation. The reference devices without any TiO_2 (wo) and those with TiO_2 (w), all based on four bilayers of PDDA-PSS, showed similar voltage buildup variation in response to the excitation with different intensities at different wavelengths. In neither of the devices (wo/w), we did not observe any considerable improvement in the outputs, which implies that TiO_2 layer did not significantly affect the charge transfer mechanism. In these structures, the electrons are not able to migrate to the TiO_2 layer.

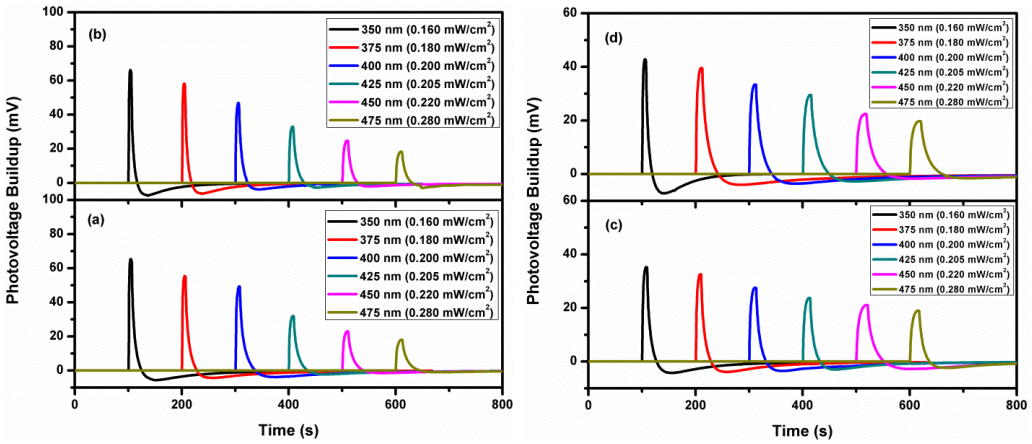

Figure 8.3.1 Variations of the photovoltage buildup based on four bilayers PDDA-PSS at different excitation wavelengths (a) without TiO_2 and (b) with TiO_2. Photovoltage buildup variation based on one bilayer PDDA-PSS (c) without TiO_2 and (d) with TiO_2.

We suggest that one primary mechanism responsible for hindering the electron transfer to the TiO_2 layer in our device design structure might be the blocking of electron transfer due to the thickness of the polyelectrolyte polymers (PDDA-PSS). As shown in Figure 8.1.1(a), the conduction band edge for the CdTe NCs lies above that of TiO_2. As a result, electron injection into TiO_2 layer should be strongly favored. Of crucial interest, we attribute the similar voltage buildup variation in the devices wo/w TiO_2 layer to the thickness of polyelectrolyte polymers. When the polyelectrolyte polymers are so thick that they prevent electron transfer to the TiO_2 layer, electrons are trapped inside the NCs. Trapped electrons may recombine with the photogenerated holes at the interface of NCs and Al layer. As a result, a similar amount of voltage buildup compared to the reference devices can be observed. Furthermore, when we used the generic definition of sensitivity (S = V/P) as the ratio of voltage buildup (V) to the incident optical power (P), again no considerable change was observed as shown in Figure 8.3.2(a).

In the case that the dielectric polyelectrolyte is thin enough, electrons are not completely trapped inside the NCs. Instead, they can be transferred to the TiO_2 as the electron accepting layer. Consequently, recombination probability of

photogenerated excitons in the NCs decreases, resulting in larger photovoltage buildup. Due to the change in the surface coverage of the NCs as the number of polyelectrolyte bilayers increases, an individual control sample for each set has been fabricated. Decreasing the number of polyelectrolyte polymers from four to one bilayer, the enhanced electron injection into TiO_2 layer is confirmed by the voltage buildup spectra, which exhibits a great enhancement, in Figure 8.3.1(c-d). This finding suggests the possibility of photogenerated electron transfer to the TiO_2 layer. In the presence of the thin polyelectrolyte polymer between the NCs and TiO_2, electron transfer to the TiO_2 film takes place easily, which in turn decreases the recombination probability of the electrons and holes in the NCs. As a result, a larger voltage buildup can be observed, which consequently enhances the device sensitivity, as shown in Figure 8.3.2(b). Here, we observed the sensitivity enhancement over a broad spectral range (350-475 nm) up to 22% compared to the reference sample. Furthermore, the sensitivity enhancement at longer wavelengths is not larger than the shorter wavelengths. This evidence supports that the enhancement is most likely because of the charge transfer mechanism and there is no absorption enhancement of CdTe NC monolayer. Indeed, CdTe NCs show weaker absorption at longer wavelength and, if there was higher sensitivity enhancement in this spectral range, then we could attribute the enhancement to the increase in optical absorption of CdTe NC monolayer. However, we clearly observe a higher enhancement at shorter wavelengths, which we attribute to the electron transfer from CdTe NCs to TiO_2 thin film. Furthermore, a slight enhancement in both of the wo/w device performance at the longer wavelengths can be attributed to the lower photon energies. These low energetic electrons are less probable to pass the potential barrier of the NCs and more probable to be captured at the surface states.

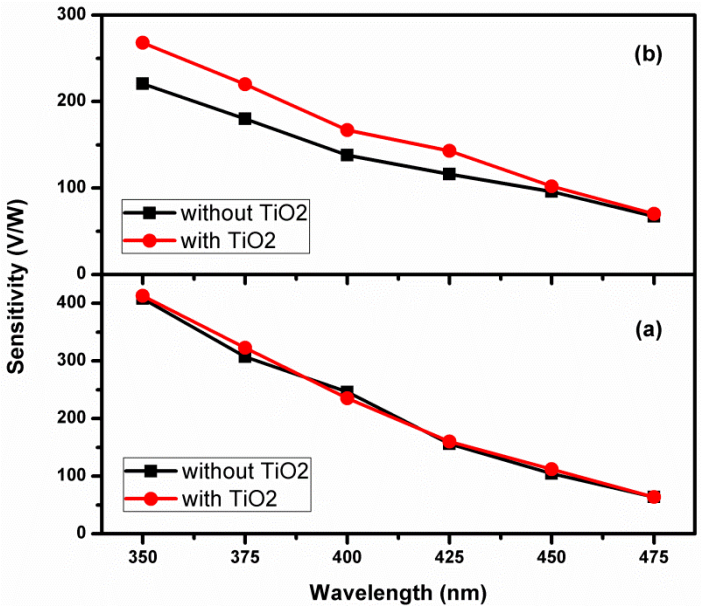

Figure 8.3.2 Sensitivity comparison of the LS-NS devices in the absence and presence of TiO_2 layer for the structures based on (a) four bilayers PDDA-PSS and (b) one bilayer PDDA-PSS.

To further verify the existence of charge transfer from the NCs to the TiO_2 film, we conducted time-correlated single-photon counting experiments (Picoquant, Fluotime 200) on the hybrid structure composed of the NC monolayer on top of the polyelectrolyte polymers coated on 10 nm TiO_2 deposited substrates and on the same structure without TiO_2. Single NC monolayer based films were prepared following the assembly of bilayers of PDDA-PSS, with the monolayer of CdTe NCs subsequently self-assembled via dip coating. These hybrid structures wo/w TiO_2 layer were subjected to TRF spectroscopy at room temperature. TRF system has a calibrated time resolution of 32 ps and a pulsed laser diode with the excitation wavelength of 375 nm. TRF detection was performed at the in-film peak emission wavelength of the NCs, which is 640 nm. Figure 8.3.3 depicts the TRF decay curves for the entire samples wo/w TiO_2 layer. The decay curves were fitted with multi-exponentials ($\chi 2 \sim 1$) and the excited-state lifetimes for the samples wo/w TiO_2 were calculated via amplitude-averaging since there is only one type of fluorophore (i.e., the NCs) in the system. As evident from the figure, there is a clear difference between TRF

decays of the one bilayer PDDA-PSS based structures wo/w TiO_2 layer. According to the measurement, the amplitude-averaged lifetime decreases considerably from 0.796 ns in the sample without any TiO_2 to 0.467 ns in the sample with TiO_2. This reduction in the lifetime supports the presence of electron transfer channel from the donor NCs into the acceptor TiO_2. Here it is worth noting that due to the lack of overlap between the TiO_2 absorption and the NC emission, the energy transfer from NCs to TiO_2 is ruled out in this work [88]. Similarly, to verify the device demonstration in which the thick polyelectrolyte layers such as four bilayers PDDA-PSS prevent the electron transfer from the NCs to the TiO_2 layer, we took the TRF measurements of the structures with a monolayer of CdTe NCs using four bilayers PDDA-PSS wo/w TiO_2.

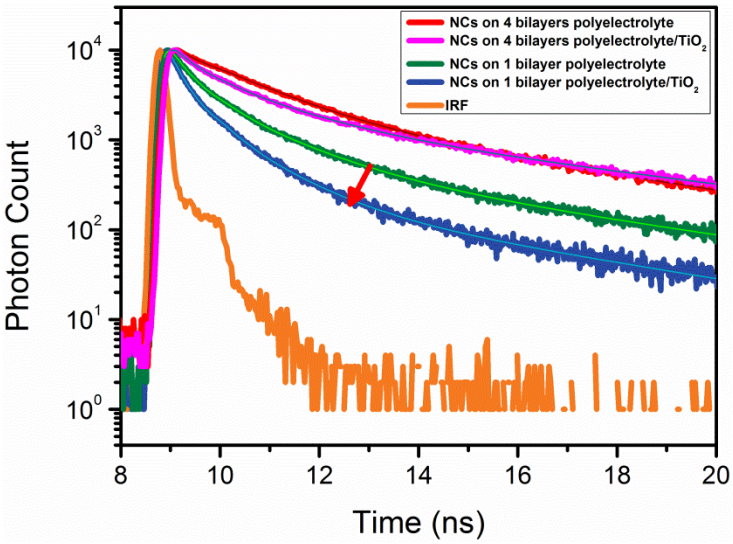

Figure 8.3.3 Time-resolved PL decays of the NCs in the absence and presence of TiO_2 layer based on different bilayers of polyelectrolyte polymers. The arrow indicates the reduction in the lifetime of the NC samples based on one bilayer of polyelectrolyte polymers from the structure without TiO_2 to the one with the TiO_2 layer.

Lifetimes of the structures based on four bilayers of PDDA-PSS wo/w TiO_2 were found to be very similar to each other, which is ~1.74 ns. Thick polyelectrolyte polymers must therefore hinder the migration of electrons to the

TiO_2 film, which explains the observation of no performance improvement in device operation aforementioned. For the further analysis of the lifetimes, the electron transfer rate of the presented structures was calculated by using the expression $\gamma_{ET} = \gamma_{hybrid} - \gamma_{ref}$ [89], where γ_{hybrid} is the rate for the single monolayer NCs on top of bilayers of polyelectrolyte polymers with the presence of TiO_2 and γ_{ref} is the NCs excited-state relaxation rate obtained from the same structure without any TiO_2. By subtracting the rate of the hybrid structure from that of the reference for the one bilayer based PDDA-PSS, we predicted an electron transfer rate of $\gamma_{ET} = 0.89\,\mathrm{ns}^{-1}$. However, this rate is almost zero for the four bilayers case. Furthermore, we calculated the electron transfer efficiency using the relation $\eta = \gamma_{ET} / (\gamma_{ET} + \gamma_{ref})$ and the resulting efficiency for the one bilayer case was found to be 41.3%. This significant efficiency explains the migration of a considerable amount of photogenerated electrons from the CdTe NCs to the TiO_2 layer. These observations are in strong agreement with the voltage buildup and sensitivity spectrum of the LS-NS with TiO_2.

Chapter 9

Multiple Exciton Generation and Charge Accumulation from Photosensors of CdHgTe Monolayer Nanocrystals

9.1 Introduction

In this chapter, we study sensitivity enhancement in LS-NS devices via multi exciton generation (MEG). MEG corresponds to multiple electron-hole pairs generated per photon when the photon energy exceeds the MEG threshold. MEG threshold can be calculated as

$$E_{Photon} / E_{Bandgap} \succ \left(2 + \frac{m_e}{m_h} \right) \tag{5}$$

where E_{photon} is the photon energy, $E_{bandgap}$ is the band gap energy of NC, and m_h and m_e are the effective masses of hole and electron, respectively. MEG converts the excess energy of the high energy photon to extra electron-hole pair generation, and thus increases the device efficiency [90, 91].

In this work we propose the use of MEG to enhance the electron-hole pair generation and subsequent charge accumulation in the CdHgTe monolayer of the LS-NS device. Subsequently, a larger number of electrons are likely to be trapped inside the NCs while holes accumulate at the metal contact. We fabricated LS-NS devices from three different sets of NCs for comparative study. Two different CdHgTe NCs (MPA and TGA ligands) have been investigated as candidate materials for MEG enhancement. These NCs have a suitable exciton absorption peak, which enables them to be used for the MEG absorber device. Being aware of the improper band gap of CdTe NCs for MEG to the corresponding excitation spectra, we use this LS-NS device based on these NCs as the control sample where MEG does not take place.

9.2 Experiments

Colloidal water soluble MPA and TGA ligand CdHgTe NCs were synthesized in accordance with [92] with the first exciton peak at wavelengths of 835 and 950 nm, respectively. Figure 9.2.1(a) shows the high-resolution transmission electron microscopy (HRTEM) image of the MPA ligand CdHgTe NCs with the 6 nm in size. Furthermore, aqueous CdTe NCs were synthesized with an excitonic absorption peak at around 605 nm corresponding to a diameter of ~ 3.7 nm. Figure 9.2.1(a) demonstrates optical absorption spectra of the resulting NCs. Also a schematic of the proposed LS-NS devices is shown in Figure 9.2.1(b). After cleaning the indium tin oxide (ITO) substrate, a 50 nm thick high dielectric constant HfO_2 film deposited via ALD on the 1 cm × 0.75 cm area. Because of using pulses water, ALD preferentially coats hydrophilic surfaces, which helps to improve the dip-coated film quality. Subsequently, in order to deposit a highly closed packed monolayer of NCs on the substrate, poly (diallyldimethylammonium chloride) (PDDA) and poly (sodium 4-styrenesulfonate) (PSS) bilayers were dip-coated to build four bilayers using layer-by-layer assembly. Finally, Al contact was laid down immediately on top of the CdHgTe NCs monolayer by using an electron beam evaporator. After

device fabrication, voltage-time (V-t) characteristics and sensitivity were taken to characterize without applying any external bias. During these measurements, the samples were grounded from the ITO contact, connected in series with a load resistance of 200 MΩ.

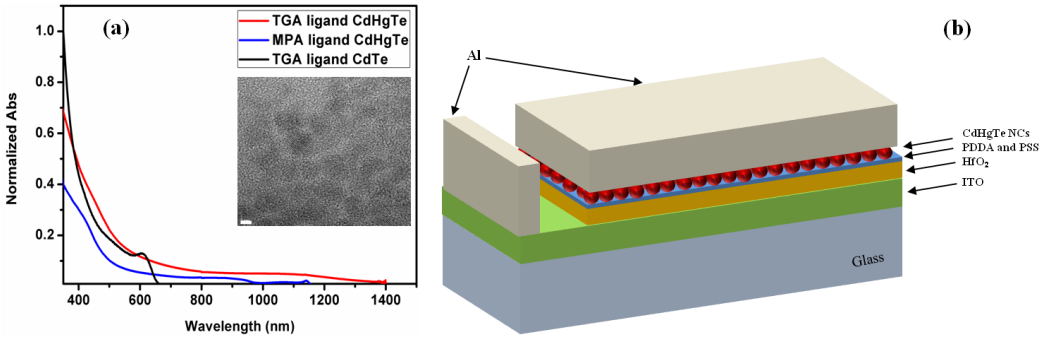

Figure 9.2.1 Absorption spectra of NCs and device structure. (a) UV-vis absorption spectrum of aqueous TGA and MPA ligand CdHgTe and CdTe NCs at room temperature. (b) Schematic drawing of the light-sensitive nanocrystal skin structure. Monolayer CdHgTe NCs were formed through dip-coating procedure.

To measure the effect of MEG on LS-NS devices, they were illuminated via a Xenon lamp light source and a monochromator was used to provide tunable wavelength source from 350 to 550 nm. The number of absorbed photons at each wavelength was adjusted to make the absorbance of CdHgTe NCs to be identical for all corresponding wavelengths.

9.3 Results and Discussions

For the LS-NS devices based on the monolayer of MPA ligand CdHgTe, MEG occurred at over 2.03 times of the excitonic energy of the NCs (1.48 eV) which correspond to 3.02 eV in energy or 411 nm in wavelength. Subsequently, the voltage buildup and sensitivity spectra shown in Figure 9.3.1 reveal no change up to the MEG threshold and approximately remain constant. However, for the wavelength of < 425 nm towards UV the sensitivity rises sharply. As it can be seen, the sensitivity enhance by ~3.3-folds at 350 nm wavelength with respect to

the long wavelengths where MEG does not occur. Similarly, these results of LS-NS device based on a monolayer of TGA ligand CdHgTe NCs are consistent with the role of MEG. In this device, due to the larger band gap (with the first exciton peak at a wavelength of 950 nm) the threshold of MEG is at a longer wavelength, around 468 nm. The spectral sensitivity and potential buildup of the devices show a jump in the sensitivity at the vicinity of MEG threshold in agreement with the previous device, indicating the multiple electron-hole pair generation of LS-NS devices. A slight change in the overall sensitivity of the two devices can be attributed to the size of NCs and their ligand length.

The observed voltage buildup spectra of the two samples exhibit over two times enhancement in charge generation for photon energies below the MEG threshold. We correlate these observations with the probability of charge trapping in NCs. For our design structure, photon energies of excited photons together with the ligand length and the size of NCs may all influence the trap state occupation. During measurements, since the number of absorbed photons is adjusted to be the same, the deeper trap states dominate the sensitivity at low photon energies (long wavelengths) resulting in a lower voltage buildup. Increasing photon energies (lower wavelengths) leads saturation of deeper and shallower trap states. This translates to an effective increase in the voltage buildup and consequently the sensitivity.

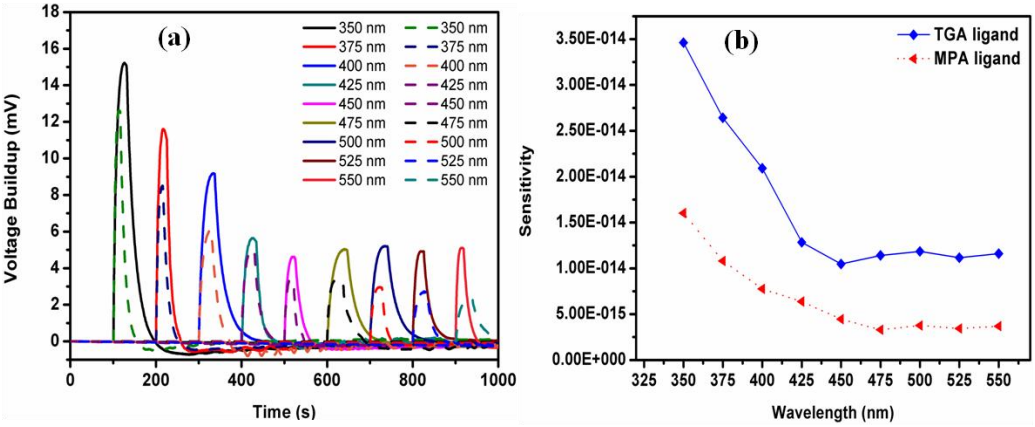

Figure 9.3.1 (a) Voltage buildup behavior of LS-NS devices based on a monolayer of TGA (solid line) and MPA (dashed line) ligand CdHgTe NCs at different wavelengths. (b) Spectral sensitivity of two LS-NS devices corresponding to their voltage buildup while identical numbers of photons impinge on them.

Implementing a proof-of-concept, demonstration for trapping charges we built a LS-NS device from a monolayer of CdTe NCs having a large enough band gap energy to prevent MEG and adequately small in size to prove the concept of trapped charges. Accordingly, the device characterization did not show any sharp increase in the photogenerated potential buildup and sensitivity at different wavelengths (see Figure 9.3.2). Indeed, a monotonous increase in the sensitivity toward the UV spectral range was observed. This observation agrees with our hypothesis on the effect of photon energies in sensitivity and voltage buildup. This suggests that E_{photon} influence the trapping efficiency. Higher photon energies excite electrons to deeper and shallower trap states, allowing for more holes to accumulate in the metal contact. As the NCs size increases, the probability of surface trap charge decreases. Consequently, small NCs are more probable to trap charges. Since CdTe NCs were 3.7 nm in size, for such a small NCs, the probability of electrons being trapped is more than large NCs. Consequently, we observed higher sensitivity. Accordingly, for the LS-NS based on these small NCs, more electrons are trapped, which means more holes accumulate at the metal contact, resulting in higher sensitivity.

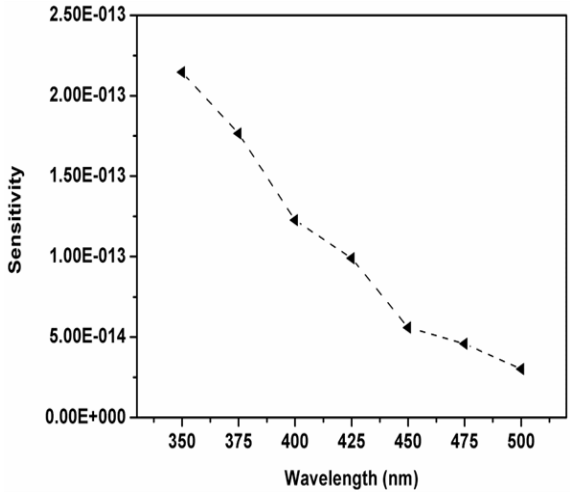

Figure 9.3.2 Sensitivity of the LS-NS based on a monolayer of CdTe NCs at corresponding wavelength.

Furthermore, the occurrence of MEG in the LS-NS design structure confirms that multiple charge generation occurs faster than the capture of the excited carrier being trapped. While, the device operation is based on the electron trapping, multiple carrier generation and hole accumulation takes place before they are captured by the traps. Consequently, after this multiple charge generation, electrons are trapped at the available states and holes accumulate at the electrode.

Chapter 10

Conclusion

In this thesis, we proposed and demonstrated highly efficient, semi-transparent, large-area, solution processable NC-based photosensors employing only single monolayers of NCs. These devices operate on the basis of photogenerated charge accumulation for which there is no need for external biasing (though an external bias also be applied to quickly reset the system if desired). The monolayer of CdTe NCs, placed exactly underneath the metal contact without any transit intervening layer, results in close interaction enabling high photosensitivity and high stability under ambient conditions because of the device architecture sealing the NC monolayer. Furthermore, this device architecture is advantageous in terms of using a small amount of NC materials and making the device transparent with sufficient partial optical absorption. With the ligand removal, we observed substantial enhancement of ~ 73% in the light sensitivity and 3-fold faster response with respect to the case of using ligands. Also, we obtained a significant decrease in the minimum noise equivalent intensity by a factor of 4.4 in the case of ligand-removed NC devices (0.443 $\mu W/cm^2$) compared to the devices without ligand removal (1.94 $\mu W/cm^2$).

In the following chapters we presented that using LSP the photosensitivity of NC monolayer light-sensitive skins can be either enhanced or suppressed and

their operational wavelength region can be accordingly extended or curtailed where the optical absorption is not sufficient for charge generation. The measured voltage buildup spectra clearly reveal the influence of the silver nanoparticles on the optical absorption and charge generation in LS-NS devices. Moreover, to disclose the effect of localized plasmonics in the vicinity of metallic nanostructures, we studied the distance dependent sensitivity with silver nanoparticles incorporated at varying distances to NC skins. Likewise, the plasmonic nanostructure can also be tuned well to enhance the photosensitivity of the light-sensitive devices into the infrared region if desired.

Additionally, we reported broadband highly sensitive, solution processed and semi-transparent tandem photosensitive skin through the incorporation of single colloidal monolayers of CdHgTe and CdTe NCs. With the addition of a CdHgTe junction to the existing CdTe one, enhancement in sensitivity and spectral range extension were observed. Furthermore, due to the higher absorption coefficient of CdHgTe monolayers, illumination from the top side was detected to be more efficient compared to the bottom one. The present tandem PNS concept can be used to build photosensitive devices with three or more junctions. Such many-junction devices provide a route to enhance the sensitivity and increase the devices operation probability.

We also showed photosensitive NC skins utilizing a band gap gradient of cascaded NC layers exhibit significant sensitivity enhancement and extension in their operating wavelength range. This performance improvement is attributed to exciton transfer from the layer with the smallest NCs to the layer with the largest NCs. In this work, by conducting TRF measurements of NC structures, we observe and attribute the reduction in average PL lifetime of the smallest NCs and the increase in PL lifetime of the largest NCs compared to the lifetimes of the same NCs in the hybrid sample to exciton transfer through the NC layers. These observations strongly coincide with the measured sensitivity enhancement and operating wavelength range extension.

We also studied the transporting of photogenerated electrons to the TiO_2 layer in light-sensitive skins, which leads to great enhancement in device sensitivity. We observed that using TiO_2 layer the sensitivity of LS-NS devices can be enhanced or remain unaffected depending on the thickness of the polyelectrolyte polymers. Subsequently, we verified that thick polyelectrolyte polymer layers prevent transferring the photogenerated electrons to the TiO_2 layer. Consequently, we designed our optimum structure based on one bilayer PDDA-PSS to improve the charge separation at the CdTe/TiO_2 interface. The measured voltage buildup spectra clearly reveal the influence of TiO_2 layer and charge transporting in the LS-NS devices. Also, we studied the influence of TiO_2 layer and tracked changes in the TRF decay of the structures with a monolayer of CdTe NCs based on different polyelectrolyte polymer thicknesses. We attribute the shortening of lifetimes to the presence of electron transfer from NCs to TiO_2, which is energetically favorable.

Finally, light-sensitive devices based on a monolayer of CdHgTe NCs film were made to demonstrate sensitivity enhancement due to MEG. In particular, the numbers of trapped electrons and extracted holes were shown to be increased per absorbed photon. We hypothesize that the size of the NCs, photon energies and ligand length affect the probability of charge trapping in the NCs. As a result, voltage buildup may enhance more than expected results in the presence of MEG or steady increase in the absence of MEG. However, sharp rises in voltage buildup and sensitivity at the threshold of NCs, support the charge extraction efficiency via MEG. Our findings presented herein have significant implications for the future design of optical sensing applications and moving toward new-generation light harvesting devices.

Below is given a list of SCI journal publications and international conferences that resulted from this thesis research and related work during my graduate study at Bilkent University.

- H. V. Demir, **S. Akhavan**, B. Guzelturk, "Large-area light-sensitive nanocrystal skins and manufacturing method," patent pending.

- **S. Akhavan,** B. Guzelturk, V. K. Sharma, and H. V. Demir, "Large-area semi-transparent light-sensitive nanocrystal skins," ***Optics Express*** 20 (23) 25255-25266 (2012).

- **S. Akhavan,** K. Gungor, E. Mutlugun, and H. V. Demir, "Plasmonic light-sensitive skins of nanocrystal monolayers," ***Nanotechnology*** 24 155201 (2013). *IOP SELECT*
  Highlighted in Nanotechweb

- **S. Akhavan** et al., "Flexible Semi-Transparent Tandem Photosensitive Nanocrystal Skins," *in submission.*

- **S. Akhavan** et al., "Nanocrystal skins with exciton funneling for photosensing," *in review.*

- **S. Akhavan** et al., "Photosensitivity enhancement in semi-transparent light-sensitive skins of nanocrystal monolayers with electron transfer to TiO_2," *in submission.*

- **S. Akhavan** et al., "Multiple exciton generation and charge accumulation from photosensors of CdHgTe monolayer nanocrystals," *in submission.*

- U. O. S. Seker, V. K. Sharma, **S. Akhavan**, and H.V. Demir, "Bioengineered Peptides for Nanohybrid Assemblies," *under revision.*

- **S. Akhavan**, B. Guzelturk, V. K. Sharma, and H. V. Demir, "Large-area semi-transparent light-sensitive nanocrystal skins," Proceeding of IEEE Photonics Society 2012 Annual Meeting (LEOS 2012), Burlingame, California, USA.

- **S. Akhavan**, K. Gungor, and H. V. Demir, "Plasmonic nanoparticle enhanced sensitivity of light-sensitive nanocrystal skins," Material Research Society (MRS) 2012 fall meeting, Boston, USA.

Bibliography

[1] L. M. Vatsia, “Atmospheric optical environment,” Research and Development Tech. Rep. ECOM-7023, (1972).

[2] M. Ettenberg, “A little night vision,” Adv. Imag., **20**, 29-32 (2005).

[3] X. Gao, Y. Cui, R. M. Levenson, L.W. K. Chung, and S. Nie, “In vivo cancer targeting and imaging with semiconductor quantum dots,” Nature Biotechnol. **22**, 969-976 (2004).

[4] Y. T. Lim, S. kim, A. Nakayama, N. E. Scott, M. G. Bawendi, and J. F. Frangoini, “Selection of quantum dot wavelengths for biomedical arrays and imaging,” Molec. Imag. **2**, 50-64 (2003).

[5] S. Kim, Y. T. Lim, E. G. Soltesz, A. M. De Grand, J. Lee, A. Nakayama, J. A. Parker, T. Mihaljevic, R. G. Laurence, D. M. Dor, L. H. Cohn, M. G. Bawendi, and J. V. Frangioni, “Near-infrared fluorescent type II quantum dots for sentinel lymph nod mapping,” Nature Biotechnol., **22**, 93–97 (2004).

[6] T. Hoetler, “Broad spectrum performance via VisGaAs,” Adv. Imag., vol. **18**, 14–19 (2003).

[7] C. B. Les, “Image sensor market: Changing, but moving upward,” Photonics Spectra, **43**, 27–28 (2009).

[8] A. El Gamal, and H. Eltoukhy, “CMOS image sensors,” IEEE Circuits Devices Mag. **21**, 6–20 (2005).

[9] C. M. Herzinger, B. Johs, W. A. McGahan, J. A. Woollam, and W. Paulson, "Ellipsometric determination of optical constants for silicon and thermally grown silicon dioxide via a multi-sample, multi-wavelength, multi-angle investigation," J. Appl. Phys. **83**, 3323–3336 (1998).

[10] K. Minoglou, et al. "Reduction of electrical crosstalk in hybrid backside illuminated CMOS imagers using deep trench isolation," 2008 IEEE Int. Interconnect Technol. Conf. 129–131 (2008).

[11] S. V. Gaponenko, *Introduction to Nanophotonics* (Cambridge University Press, 2010).

[12] T. Erdem and H. V. Demir, "Semiconductor nanocrystal as rare-earth alternatives," Nat. Photonics, **5**, 126 (2011).

[13] T. Erdem and H. V. Demir, "Color science of nanocrystal quantum dots for lighting and displays," Nanophotonics, **2**, 57-81 (2013).

[14] X. Lan, J. Bai, S. Masala, S. M. Thon,Y. Ren, I. J. Kramer, S. Hoogland, A. Simchi, G. I. Koleilat, D.Paz-Soldan, Z. Ning, A. J. Labelle, J. Young Kim, G. Jabbour, and E. H. Sargent, "Self-assembled, nanowire network electrodes for depleted bulk heterojunction solar cells," Adv. Mater., **25**, 1769-1773 (2013).

[15] G. Konstantatos, and E. H. Sargent, "Nanostructured materials for photon detection," Nature Nanotechnol., **5**, 391-400 (2010).

[16] G. Konstantatos, M. Badioli, L. Gaudreau, J. Osmond, M. Bernechea, F. P. G. de Arquer, F. Gatti, and F. H. L. Koppens, "Hybrid graphene-quantum dot phototransistors with ultrahigh gain," Nat. Nanotechnol. **7**, 363-368 (2012).

[17] X. Michalet, F. F. Pinaud, L. A. Bentolila, J. M. Tsay, S. Doose, J. J. Li, G. Sundaresan, A. M. Wu, S. S. Gambhir, and S. Weiss, "Quantum dots for live cells, in Vivo imaging, and diagnostics," Science, **307**, 538-544 (2005).

[18] P. Alivisatos, "The use of nanocrystals in biological detection," Nat. Biotechnol. **22**, 47-52 (2004).

[19] G. Konstantatos, I. Howard, A. Fischer, S. Hoogland, J. Clifford, E. Klem, L. Levina, and E. H. Sargent, "Ultrasensitive solution cast quantum dot photodetectors," Nature, **442**, 180-183 (2006).

[20] F. Prins, M. Buscema, J. S. Seldenthuis, S. Etaki, G. Buchs, M. Barkelid, V. Zwiller, Y. Gao, A. J. Houtepen, L. D. A. Siebbeles, and H. S. J. van der Zant, **"**Fast and efficient photodetectors in nanoscale quantum dot junctions,**"** Nano Lett., **12**, 5740-5743 (2012).

[21] J. P. Clifford, G. Konstantatos, K. W. Johnston, S. Hoogland, L. Levina, and E. H. Sargent, "Fast, sensitive and spectrally tuneable colloidal-quantum-dot photodetectors," Nat. Nanotechnol., **4**, 40-44 (2009).

[22] E. L. Dereniak, G. D. Boreman *Infrared Detectors and Systems* (Wiley & Sons, New York, 1996).

[23] T. Franzl, T. A. Klar, S. Schietinger, A. L. Rogach, J. Feldmann, "Exciton recycling in graded gap nanocrystal structures," Nano Lett., **4**, 1599-1603 (2004).

[24] M. G. Bawendi, M. L. Steigerwald, and L. E. Brus, "The quantum mechanics of larger semiconductor clusters ('Quantum Dots')," Annual Review of Physical Chemistry, **41**, 477-496 (1990).

[25] A. Alivisatos, “Perspectives on the physical chemistry of semiconductor nanocrystals,” Journal of Physical Chemistry, **3654**, 13226-13239 (1996).

[26] N. Gaponik, S. G. Hickey, D. Dorfs, A. L. Rogach, and A. Eychmüller, “Progress in the light emission of colloidal semiconductor nanocrystals,” small, **6**, 1364-1378 (2010).

[27] J. van Embden, J. Jasieniak, and P. Mulvaney, “Mapping the optical properties of CdSe/CdS heterostructure nanocrystals: the effects of core size and shell thickness,” JACS, **131**, 14299-14309 (2009).

[28] S. H. Wei, A. Zunger, “Calculated natural band offsets of all II–VI and III–V semiconductors: Chemical trends and the role of cation d orbitals,” Appl. Phys. Lett., **72**, 2011-2013 (1998).

[29] A. Mews, A. Eychmüller, M. Giersig, D. Schooss, and H. Weller, “Preparation, characterization, and photophysics of the quantum dot quantum well system cadmium sulfide/mercury sulfide/cadmium sulfide,” J. Phys. Chem., **98**, 934–941 (1994).

[30] X. H. Zhong, R. G. Xie, Y. Zhang, T. Basche, and W. Knoll, “High-quality violet- to red-emitting ZnSe/CdSe core/shell nanocrystals,” Chem. Mater., **17**, 4038–4042 (2005).

[31] D. V. Talapin, A. L. Rogach, I. Mekis, S. Haubold, A. Kornowski, M. Haase, “Synthesis and Surface Modification of Amino-Stabilized CdSe, CdTe and InP Nanocrystals,” H. Weller. Coll. Surf. A, **202**, 145-154 (2002).

[32] P. Reiss, M. Protière, and L. Li, "Core/Shell Semiconductor Nanocrystals," Small, **5**, 154-168, (2009)

[33] H. V. Demir, S. Nizamoglu, T. Erdem, E. Mutlugun, N. Gaponik, and A. Eychmüller, "Quantum dot integrated LEDs using photonic and excitonic color conversion," Nano Today, **6**, 632-647 (2011).

[34] E. H. Sargent, "Colloidal quantum dot solar cells," Nature Photon., **6**, 133-135 (2012).

[35] G. Konstantatos, and E. H. Sargent, "Nanostructured materials for photon detection," Nature Nanotech., **5**, 391-400 (2010).

[36] S. A. McDonald, G. Konstantatos, S. Zhang, P. W. Cyr, E. J. D. Klem, L. Levina, and E. H. Sargent, "Solution-processed PbS quantum dot infrared photodetectors and photovoltaics," Nature Mater., **4**, 138-142 (2005).

[37] H. V. Demir, S. Nizamoglu, E. Mutlugun, T. Ozel, S. Sapra, N. Gaponik, and A. Eychmüller, "Tuning shades of white light with multi-color quantum-dot-quantum-well emitters based on onion-like CdSe-ZnS heteronanocrystals," Nanotechnology, **19**, 335203 (2008).

[38] N. Cicek, S. Nizamoglu, T. Ozel, E. Mutlugun, D. U. Karatay, V. Lesnyak, T. Otto, N. Gaponik, A. Eychmüller, and H. V. Demir, "Structural tuning of color chromaticity through nonradiative energy transfer by interspacing CdTe nanocrystal monolayers," Appl. Phys. Lett. **94**, 061105 (2009).

[39] S. Nizamoglu, E. Mutlugun, O. Akyuz, N. K. Perkgoz, H. V. Demir, L. Liebscher, S. Sapra, N. Gaponik, and A. Eychmüller, "White emitting CdS quantum dot nanoluminophores hybridized on near-ultraviolet LEDs for high

quality white light generation and tuning," New J Phys, **10**, 023026 (2008).

[40] E. Mutlugun, I. M. Soganci, and H. V. Demir, "Nanocrystal hybridized scintillators for enhanced detection and imaging on Si platforms in UV," Opt. Express **15**, 1128-1134 (2007).

[41] C. B. Murray, D. J. Noms, and M. G. Bawendi, "Synthesis and characterization of nearly monodisperse CdE (E = S, Se, Te) semiconductor nanocrystallites," J . Am. Chem. Soc **115**, 8706-8715 (1993).

[42] J. M. Luther, M. Law, M. C. Beard, Q. Song, M. O. Reese, R. J. Ellingson, and A. J. Nozik, "Schottky solar cells based on colloidal nanocrystal films," Nano Lett., **8**, 3488-3492 (2008).

[43] J. Zhao, J. A. Bardecker, A. M. Munro, M. S. Liu, Y. Niu, I.-K. Ding, J. Luo, B. Chen, A. K.-Y. Jen, and D. S. Ginger, "Efficient CdSe/CdS quantum dot light-emitting diodes using a thermally polymerized hole transport layer," Nano Lett., **6**, 463-467 (2006).

[44] S. H. Im, Y. H. Lee, S. I. Seok, S. W. Kim, and S.-W. Kim, "Quantum-dot-sensitized solar cells fabricated by the combined process of the direct attachment of colloidal CdSe quantum dots having a ZnS glue layer and spray pyrolysis deposition," Langmuir, **26**, 18576-18580 (2010).

[45] T.-H. Kim, K.-S. Cho, E. K. Lee, S. J. Lee, J. Chae, J. W. Kim, D. H. Kim, J.-Y. Kwon, G. Amaratunga, S. Y. Lee, B. L. Choi, Y. Kuk, J. M. Kim, and K. Kim, "Full-colour quantum dot displays fabricated by transfer printing," Nature Photon., **5**, 176–182 (2011).

[46] D. Yu, C. Wang, B. Wehrenberg, and P. Guyot-Sionnest, "Variable Range Hopping Conduction in Semiconductor Nanocrystal Solids," Phys. Rev. Lett., **92**, 216802 (2004).

[47] A. Pandey, and P. Guyot-Sionnest, "Slow Electron Cooling in Colloidal Quantum Dots," Science, **322**, 929-932 (2008).

[48] V. I. Klimov, "Optical Gain and Stimulated Emission in Nanocrystal Quantum Dots," Science, **290**, 314-317 (2000).

[49] D. V. Talapin and C. B. Murray, "PbSe nanocrystal solids for n- and p-channel thin film field-effect transistors," Science, **310**, 86-89 (2005).

[50] H. Y. Chen, M. K. F. Lo, G. Yang, H. G. Monbouquette, and Y. Yang, " Nanoparticle-assisted high photoconductive gain in composites of polymer and fullerene," Nat. Nanotech., **3**, 543–547 (2008).

[51] G. Konstantatos, L. Levina, A. Fischer, and E. H. Sargent, "Engineering the temporal response of photoconductive photodetectors via selective introduction of surface trap states," Nano Lett., **8**, 1446–1450 (2008).

[52] G. Konstantatos, L. Levina, J. Tang, and E. H. Sargent, "Sensitive solution-processed Bi2S3 nanocrystalline photodetectors," Nano Lett., **8**, 4002–4006 (2008).

[53] G. Konstantatos, and E. H. Sargent, "Solution-processed quantum dot photodetectors," Proceeding of the IEEE, **97**, 1666-1683 (2009).

[54] E. J. D Klem, D. D. MacNeil, P. W. Cyr, L. Levina, and E. H. Sargent, "Efficient solution-processed infrared photovoltaic cells: Planarized all-

inorganic bul heterojunction devices via inter-quantum-dot bridging during growth from solution," Appl. Phys. Lett., **90**, 183113 (2007).

[55] V. M. Agranovich, and D. L. Mills, *Surface Polaritons: Electromagnetic Waves at Surfaces and Interfaces* (North-Holland, Amsterdam, 1992).

[56] S. kawata, *Near-field Optics and Surface Plasmon Polaritons* (Springer Verlag, Berlin, 2001).

[57] K. Sonnichsen, *Plasmons in Metal Nanostructures* (Ludwig-Maximilians University of Munich, Munich, 2001).

[58] K. L. Kelly, E. Coronado, L. L. Zhao, and G. C. Schatz, "The optical properties of metal nanoparticles: the influence of size, shape, and dielectric environment," J. Phys. Chem. B., **107**, 668-677 (2003).

[59] U. Kreibig, and M. Vollmer, *Optical Properties of Metal Clusters* (Springer Verlag, Berlin, 1995).

[60] L. M. Liz-Marzan, "Tailoring surface plasmons through the morphology and assembly of metal nanoparticles," Langmuir, **22**, 32-41 (2006).

[61] R. C. Jin, Y. W. Cao, C. A. Mirkin, K. L. Kelly, G. C. Schatz, and J. G. Zheng, "Photoinduced conversion of silver nanospheres to nanoprisms," Science, **294**, 1901-1903 (2001).

[62] L. M. Liz-Marzan, M. Giersig, and P. Mulvaney, "Synthesis of nanosized gold-silica core-shell particles," J. Phys. Chem., **12**, 4329-4335 (1996).

[63] A. L. Rogach, T. Franzl, T. A. Klar, J. Feldmann, N. Gaponik, V. Lesnyak, A. Shavel, A. Eychmüller, Y. P. Rakovich, and J. F. Donegan, "Aqueous Synthesis of Thiol-Capped CdTe Nanocrystals : State-of-the-Art," J. Phys. Chem. C, **111**, 14628-14637 (2007).

[64] G. Decher, "Fuzzy Nanoassemblies: Toward Layered Polymeric Multicomposites," Science, **277**, 1232-1237 (1997).

[65] S. Keuleyan, E. Lhuillier, V. Brajuskovic, and P. Guyot-Sionnest, "Mid-infrared HgTe colloidal quantum dot photodetectors," Nature Photon., **5**, 489–493 (2011).

[66] F. Pelayo García de Arquer, F. J. Beck, M. Bernechea, and G. Konstantatos, "Plasmonic light trapping leads to responsivity increase in colloidal quantum dot photodetectors," Appl. Phys. Lett. **100**, 043101 (2012).

[67] S. Akhavan, B. Guzelturk, V. K. Sharma, and H. V. Demir, "Large-area semi-transparent light-sensitive nanocrystal skins," Opt. Express, **20**, 25255-25266 (2012).

[68] P. Anikeeva, C. Madigan, J. Halpert, M. Bawendi, and V. Bulović, "Electronic and excitonic processes in light-emitting devices based on organic materials and colloidal quantum dots," Phys. Rev. B., **78**, 085434 (2008).

[69] D. C. Oertel and M. G. Bawendi, "Photodetectors based on treated CdSe quantum dot films," Appl. Phys. Lett., **87**, 213505 (2005).

[70] H. Raether *Surface Plasmons* (Springer, Berlin, 1988).

[71] H. A. Atwater, and A. Polman, "Plasmonics for improved photovoltaic devices," Nature Mater., **9**, 205-213 (2010).

[72] S. P. Sundararajan, N. K. Grady, N. Mirin, and N. J. Halas, "Antenna-Based Optical Imaging of Single Ca^{2+} Transmembrane Proteins in Liquids," Nano Lett., **8** 624-630 (2008).

[73] V. E. Ferry, A. Polman, and H. A. Atwater, "Modeling Light Trapping in Nanostructured Solar Cells," ACS Nano, **5**, 10055-10064 (2011).

[74] M. W. Knight, H. Sobhani, P. Nordlander, and N. J. Halas, "Photodetection with Active Optical Antennas," Science, **332,** 702-704 (2012).

[75] M. L. Tseng et al., "Fast Fabrication of a Ag Nanostructure Substrate Using the Femtosecond Laser for Broad-Band and Tunable Plasmonic Enhancement," ACS Nano, **6,** 5190-5197 (2012).

[76] X. Chen, B. Jia, J. K. Saha, B. Cai, N. Stokes, Q. Qiao, Y. Wang, Z. Shi, and M. Gu, "Broadband Enhancement in Thin-Film Amorphous Silicon Solar Cells Enabled by Nucleated Silver Nanoparticles," Nano Lett., **12**, 2187-2192 (2012).

[77] S. Akhavan, K. Gungor, E. Mutlugun, and H. V. Demir, "Plasmonic light-sensitive skins of nanocrystal monolayers," Nanotechnology, **24**, 155201 (2013).

[78] J. Jasieniak, M. Califano, and S. E. Watkins, "Size-Dependent Valence and Conduction Band-Edge Energies of Semiconductor Nanocrystals," ACS Nano, **5**, 5888-5902 (2011).

[79] E. M. Likovich, R. Jaramillo, K. J. Russell, S. Ramanathan, and V. Narayanamurti, "High-Current-Density Monolayer CdSe/ZnS Quantum Dot

Light-Emitting Devices with Oxide Electrodes," Adv. Mater., **23**, 4521-4525 (2011).

[80] L. Merhari, *Hybrid Nanocomposites for Nanotechnology: Electronic, Optical, Magnetic and Biomedical Applications* (Springer, New York, 2009).

[81] A. Shavel, N. Gaponik, and A. Eychmüller, "The assembling of semiconductor nanocrystals," Euro J Inorg Chem 3613-3623 (2005).

[82] O. Kulakovich, N. Strekal, A. Yaroshevich, S. Maskevich, S. Gaponenko, I. Nabiev, U. Woggon, and M. Artemyev, "Enhanced Luminescence of CdSe Quantum Dots on Gold Colloids," Nano Lett., **2**, 1449-1452 (2002).

[83] J. W. Ostrander, A. A. Mamedov, and N. A. Kotov, "Two modes of linear layer-by-layer growth of nanoparticle-polyelectrolyte multilayers and different interactions in the layer by layer deposition, " J. Am. Chem. Soc. **123**, 1101, (2001).

[84] A. Shavel, N. Gaponik, and A. Eychmüller, "Efficient UV-Blue Photoluminescing Thiol-Stabilized Water-Soluble Alloyed ZnSe(S) Nanocrystals," J. Phys. Chem. B., **108**, 5905-5908 (2004).

[85] T. A. Klar, T. Franzl, A. L. Rogach, and J. Feldmann, "Super-efficient exciton funneling in layer-by-layer semiconductor nanocrystal structures," Adv. Mater. **17**, 769, (2005).

[86] S. Nizamoglu, P. L. Hernandez-Martinez, E. Mutlugun, D. U. Karatay, and H. V. Demir, "Excitonic enhanement of nanradiative energy transfer from a quantum well in the optical near field of enrgy gradient quantum dots," Appl. Phys. Lett., **100**, 241109, (2012).

[87] S. Jin, A. B. F. Martinson, G. P. Wiederrecht, “Reduced Heterogeneity of Electron Transfer into Polycrystalline TiO2 Films: Site Specific Kinetics Revealed by Single-Particle Spectroscopy,” J. Phys. Chem. C, **116**, 3097–3104 (2012).

[88] B. Valeur, *Molecular Fluorescence: Principles and Applications* (WILEY-VCH, 2002).

[89] T. Förster, “Intermolecular energy migration and fluorescenc,”Annual Physics, **437**, 55–75 (1948).

[90] V. Sukhovatkin, S. Hinds, L. Brzozowski, and E. H. Sargent, “Colloidal Quantum-Dot Photodetectors Exploiting Multiexciton Generation.” Science, **324**, 1542-1544 (2009).

[91] O. E. Semonin, J. M. Luther, S. Choi, H.-Y. Chen, J. Gao, A. J. Nozik, and M. C. Beard, “Peak External Photocurrent Quantum Efficiency Exceeding 100% via MEG in a Quantum Dot Solar Cell,” Science, **334**, 1530 (2011).

[92] V. Lesnyak, A. Lutich, N. Gaponik, M. Grabolle, A. Plotnikov, U. Resch-Genger, and A. Eychmüller, “One-pot aqueous synthesis of high quality near infrared emitting $Cd_{1-x}Hg_xTe$ nanocrystals,” J. Mater. Chem., **19**, 9147-9152 (2009).